Author comments on https://doi.org/10.5194/essd-2017-100-RC1, 2017

A 20-year record (1998–2017) of permafrost, active layer, and meteorological conditions at a High Arctic permafrost research site (Bayelva, Spitsbergen): an opportunity to validate remote sensing data and land surface, snow, and permafrost models

by Julia Boike et al.

Anonymous Referee #1
Received and published: 28 November 2017

RC: Referee comment | **AC**: Author comment | **CM**: Change in the manuscript

RC1.01: Title: Consider a shorter title; only use e.g the first part: A 20-year record (1998-2017) of permafrost, active layer, and meteorological conditions at a High Arctic permafrost research site (Bayelva, Spitsbergen)
AC1.01: We adopted the amendment proposed by the referee.
CM1.01: We changed the title as follows: A 20-year record (1998-2017) of permafrost, active layer, and meteorological conditions at a High Arctic permafrost research site (Bayelva, Spitsbergen)~~: an opportunity to validate remote sensing data and land surface, snow, and permafrost models~~

RC1.02: In the abstract (L36) and other parts of the manuscript (e.g. L104, L520) the term "climate warming" and "warming of air temperatures" are used. Better use "global warming", "atmospheric temperature rise" or so instead of "climate warming"/"warming climate". The term "climate" is defined as a statistical average of meteorological conditions and as such cannot "warm" (the expression is popular but not really scientifically correct)
AC1.02: We adopted the amendments proposed by the referee.
CM1.02: We changed the named passages as follows: L36: global warming; L104: ~~of~~ air temperature~~s~~ rise; L106: This rise; L521: soil temperature data at all depths have been rising

RC1.03: L63: After IPY new updates on changes in permafrost temperature have been published and presented in recent peer-reviewed assessments, like SWIPA2017. In addition to Romanovsky et al. (2010) I therefore suggest to add e.g. Romanovsky et al. (2017). Romanovsky V, Isaksen K, Drozdov D, Anisimov O, Instanes A, Leibman M, McGuire AD, Shiklomanov N, Smith S, Walker D, 2017. Changing permafrost and its impacts. In: Snow, Water, Ice and Permafrost in the Arctic (SWIPA) 2017. pp. 65-102. Arctic Monitoring and Assessment Programme (AMAP), Oslo, Norway.
AC1.03: We included the reference proposed by the referee.
CM1.03: We changed the named sentence as follows: Thermal degradation of permafrost over the last few decades are reported from ten available circum-Arctic boreholes (Romanovsky et al., 2010) with a recent update by Romanovsky et al. (2017).

RC1.04: L208: Replace "1989" with "1898". Consider also to include that a meteorological station was established in Ny-Ålesund already in 1969.

AC1.04: We adopted the replacement proposed by the referee.
CM1.04: We changed the named passage as follows: Climate records covering a longer period of time ~~(since 1989)~~ are available from ~~the airport in Longyearbyen, which is about 110 km from Ny-Ålesund (Nordeli et al., 2014)~~ Svalbard since 1898, with the establishment of a permanent weather station in 1911 (Førland et al. 2011).

RC1.05: L470: Replace "thermometer chain" with "thermistor chain" or "thermistor string"
AC1.05: We adopted the replacement proposed by the referee.
CM1.05: We changed the named passage as follows: the thermistor chain

RC1.06: L 479-481: Please explain more in detail why you think there is an air exchange within the casing in the uppermost 1.5 m. There are several other boreholes with similar setup and such information is important.
AC1.06: We provide further information about the differences in temperature in the two figures below. The temperature data show that the differences between borehole and active layer profile can be up to several degrees during winter (Figures R1.01. & R1.02. below). The temperatures in the borehole (50 cm) during winter are colder in comparison to the soil profile (55 cm) and follow closely the air temperature signal. This effect is still clearly observed at about 150 cm depth in winter. We assume that differences in snow cover are in part responsible for the changes between borehole and profile temperatures: the snow cover is thinner at the borehole location compared to the active layer profile observed from aerial photographs. A recently submitted study to *The Cryosphere* (Gouttevin et al., Observation and modelling of snow at a polygonal tundra permafrost site: spatial variability and thermal implications) showed that spatial variability in snow (incl. both depth and structure) could lead to soil temperature differences up to 6°C at 50 cm depth. Furthermore, differences in ground properties (texture, soil volumetric water content) between the borehole and active layer profile could also be responsible for the differences in temperatures.
Since borehole drilling, pipe fitting, refilling of the pipe (no filling or addition of liquid) is different between borehole sites, we cannot give a universal statement, but rather suggest using caution when interpreting the upper 2 m of temperature.

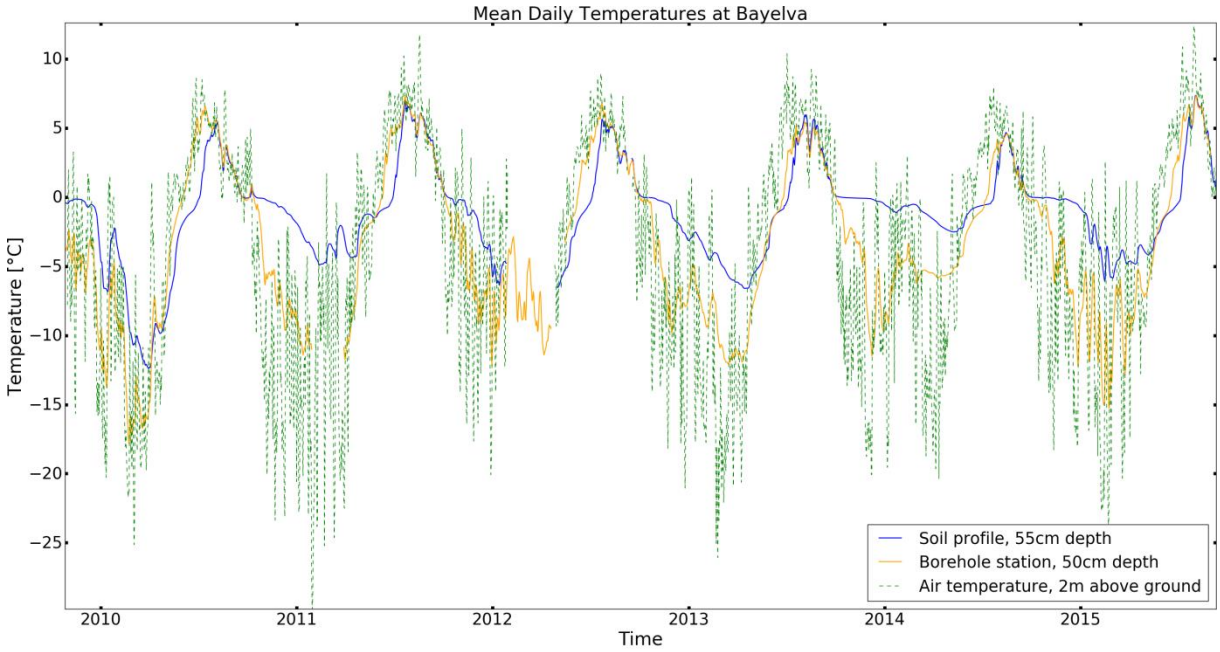

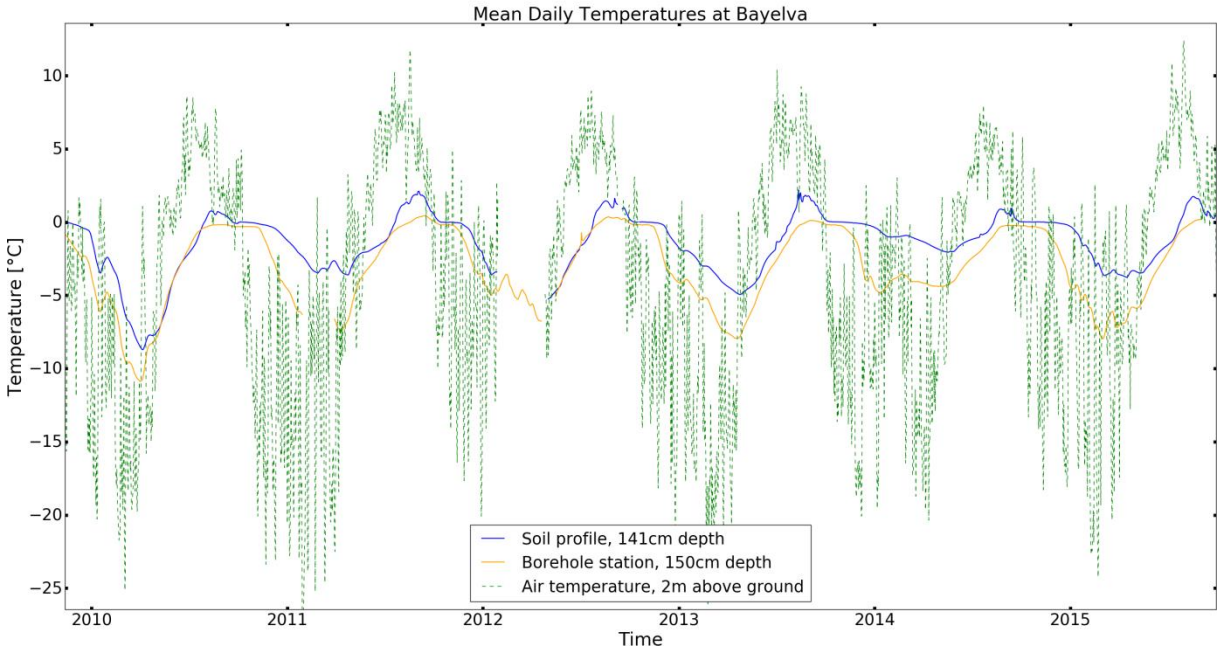

Figure R1.01. Upper: Daily mean temperature in the borehole and active layer profile at depths of 50 and 55 cm, and air temperature. **Lower:** Daily mean temperature in the borehole and active layer profile at depths of 150 and 141 cm, and air temperature.

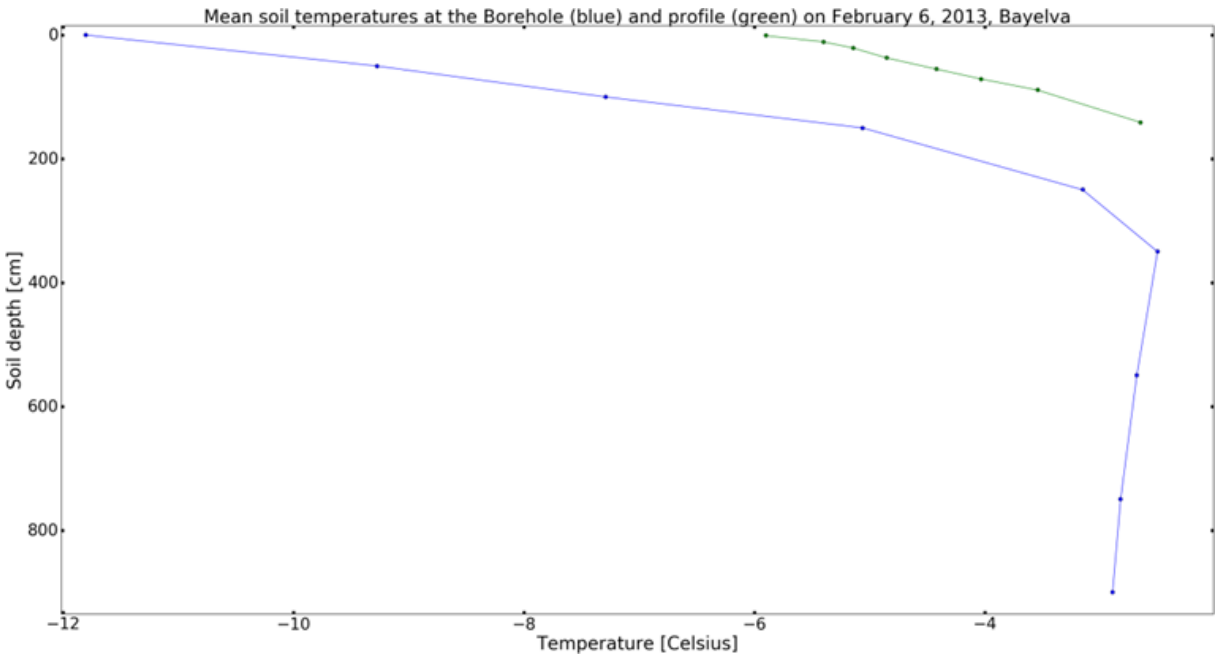

Figure R1.02. Comparison between mean borehole temperature and active layer profile on February 6, 2013.

CM1.06: We added the following information to the named passage as follows: ~~It is recommended that the temperature data from sensors installed above ground and down to a depth of 1.5 m should be used with caution because of air exchange within the casing.~~ Caution is warranted when using the borehole temperatures in the uppermost 1–2 m, since they may be affected by air movement in the borehole.

RC1.07: Figure 1: Please include exact coordinates of the Bayelva site in e.g. the figure caption.
AC1.07: We adopted the amendment proposed by the referee.
CM1.07: We added information to the text of Figure 1 as follows: Location of the Bayelva study site on Spitsbergen, western Svalbard at 78°55'15.6"N 11°49'58.5"E.

A 20-year record (1998-2017) of permafrost, active layer, and meteorological conditions at a High Arctic permafrost research site (Bayelva, Spitsbergen)~~: an opportunity to validate remote sensing data and land surface, snow, and permafrost models~~

Julia Boike[1,2], Inge Juszak[1], Stephan Lange[1], Sarah Chadburn[3,4], Eleanor Burke[5], Pier Paul Overduin[1], Kurt Roth[6], Olaf Ippisch[7], Niko Bornemann[1], Lielle Stern[6], Isabelle Gouttevin[8,9], Ernst Hauber[10], Sebastian Westermann[11]

[1] Alfred Wegener Institute Helmholtz Center for Polar and Marine Research, Telegrafenberg A43, 14473 Potsdam, Germany

[2] Geography Department Humboldt-University, Unter den Linden 6, 10099 Berlin, Germany

[3] University of Leeds, School of Earth and Environment, Leeds LS2 9JT, U.K.

[4] University of Exeter, College of Engineering, Mathematics and Physical sciences, Exeter EX4 4QF, U.K.

[5] Met Office Hadley Centre, FitzRoy Road, Exeter EX1 3PB, U.K.

[6] Institute of Environmental Physics, INF 229, University of Heidelberg, 69120 Heidelberg, Germany

[7] Institute for Mathematics, Erzstr. 1,Erzstr. 1, 38678 Clausthal-Zellerfeld, Germany

[8] Irstea, UR HHLY, centre de Lyon-Villeurbanne, 5 rue de la Doua, BP 32108, 69616 Villeurbanne Cedex, France

[9] Université Grenoble Alpes, Irstea, UR ETGR, Centre de Grenoble, 2 rue de la Papeterie-BP 76, 38402 St-Martin-d'Hères, France

[10] Institute of Planetary Research, German Aerospace Center (DLR), Rutherfordstr. 2, 12489 Berlin, Germany

[11] Department of Geosciences, University of Oslo, P.O. Box 1047, Blindern, 0316 Oslo, Norway

Correspondence to: Julia Boike (Julia.Boike@awi.de)

Abstract

Most permafrost is located in the Arctic, where frozen organic carbon makes it an important component of the global climate system. Despite the fact that the Arctic climate changes more rapidly than the rest of the globe, observational data density in the region is low. Permafrost thaw and carbon release to the atmosphere are a positive feedback mechanism that can exacerbate ~~climate~~global warming. This positive feedback functions via changing land-atmosphere energy and mass exchanges. There is thus a great need to understand links between the energy balance, which can vary rapidly over hourly to annual time scales, and permafrost, which changes slowly over long time periods. This understanding thus mandates long-term observational data sets.

Such a data set is available from the Bayelva Site at Ny-Ålesund, Svalbard, where meteorology, energy balance components and subsurface observations have been made for the last 20 years. Additional data include a high resolution digital elevation model that can be used together with the snow physical information for snow pack modeling and a panchromatic image. This paper presents the data set produced so far, explains instrumentation, calibration, processing and data quality control, as well as the sources for various resulting data sets. The resulting data set is unique in the Arctic and serves a baseline for future studies. The mean permafrost temperature is -2.8°C, with a zero-amplitude depth at 5.5 m (2009–2017). Since the data provide observations of temporally variable parameters that mitigate energy fluxes between permafrost and atmosphere, such as snow depth and soil moisture content, they are suitable for use in integrating, calibrating and testing permafrost as a component in Earth System Models. ~~The data set also includes a high resolution digital elevation model that can be used together with the snow physical information for snow pack modeling~~.

The presented data are available in the supplementary material for this paper and through the PANGAEA website (https://doi.pangaea.de/10.1594/PANGAEA.880120).

1 Introduction

Permafrost, which is defined as ground that has remained frozen continuously for two years or more, covers large parts of the land surface in the northern hemisphere, amounting to about 15 million km^2 (Brown et al., 1998). The range in temperatures and water and ice content of the upper surface layer of seasonally freezing and thawing ground (the ~~"~~active layer~~"~~) determine the biological and hydrological processes that operate in these areas. Thermal degradation of permafrost over the last few decades has been reported from ~~many~~ten available circum-Arctic boreholes Romanovsky et al., (2010) with a recent update by Romanovsky et al. (2017). Warming and thawing of permafrost and an overall reduction in the area that it covers under future climate change scenarios have been predicted in all recent climate models, but at widely varying rates (Koven et al., 2012). Continued observations, not only of permafrost thermal data but also of the multiple other types of data required to understand the changes to permafrost, are therefore of great importance. The data required includes information on the upper boundary condition of the soil (specifically on snow cover), on atmospheric conditions, and on various subsurface state variables (for example, volumetric liquid water content ~~and temperature~~). The seasonal snow cover in Arctic permafrost regions ~~can blanket~~ insulates the permafrost surface for many months of the year and has an important effect on the thermal regime of permafrost (Langer et al., 2013; López-Moreno et al., 2016). The soil's water content determines not only its hydrologic and thermal properties, but also the amount of latent heat that is either required for the seasonal thaw in spring, or produced during fall. In view of these dependencies, the ~~resulting~~ datasets (including snow cover and the thermal state of the soil and permafrost), ideally at the same resolution as any meteorological input data,

will be of great value for evaluating permafrost models (or land surface models intended for permafrost regions). In this paper we present data that incorporate subsurface components of heat and mass flux, properties of the snow cover, and weather data from the Bayelva High Arctic permafrost site.

The Bayelva research site on Spitsbergen Island in the Svalbard archipelago (78.551° N; 11.571° E) has been ~~investigated~~used for research by the AWI in collaboration with academic partners since 1998, with the original objective of developing and testing permafrost process models (Ippisch, 2001; Stern, 2017). Major developments in earth system models, for example through the European PAGE21 project (http://www.page21.org~~/~~), Permafrost Carbon Network projects (http://www.permafrostcarbon.org), and satellite calibration and validation (cal/val) missions, have subsequently led to sustained interest in the data produced from a wider modeling community. This publication provides information on the site and a full documentation of the data set collected between 1998 and 2017 that may be required for input into earth system models (Chadburn et al., 2015; Ekici et al., 2014; Ekici et al., 2015).

2 Site description

The Bayelva site is located in the European High Arctic, on western Spitsbergen in the Svalbard archipelago. It is situated about 3 km from the small village of Ny-Ålesund, which serves as a permanent hub for researchers and their logistical support. Ny-Ålesund was a coal mining area from 1916 to 1962, since then the village has been gradually transformed into a research community. Long term meteorological monitoring was initiated in 1969 by the Norwegian Sverdrup Station but research topics now also include terrestrial ecosystems,

glacier monitoring, (high Level) atmospheric research, and the Kongsfjorden ocean system, coordinated by the Ny-Ålesund Science Managers Committee (http://nysmac.npolar.no/).

The West Spitsbergen Ocean ~~Current~~, a branch of the North Atlantic ~~Current~~, warms this area to an average air temperature of between –-17.0 °C to -3.8 °C in January and from 4.6 to 6.9 °C in July (18-year period: 01 August 1993 to 31 July 2011; (Maturilli et al., 2013))~~about –13°C in January and +5°C in July~~. It also provides about 400 mm of precipitation annually, which falls mostly as snow between September and May. Significant ~~warming of~~ air temperature~~s~~ rise has been detected since 1960, which has generally been attributed to changes in the radiation budget and atmospheric circulation patterns (Førland et al., 2012; Hanssen-Bauer and Førland, 1998). This ~~warming~~rise is also reflected in the permafrost temperatures, as recorded from deep boreholes ~~(up to 102 m deep)~~ in the mountains at Janssonhaugen (Isaksen et al., 2007a; Isaksen et al., 2001; Isaksen et al., 2007b). For the 6-year period from 1999 to 2005 the borehole temperatures have increased: at 25 m by 0.26 °C, at 30 m by 0.19 °C and at 40 m by between 0.07 and 0.09 °C (Romanovsky et al., 2017). Continuous permafrost underlies the un-glaciated coastal areas to a depth of about 100 m and the active layer thickness (ALT) at the end of summer ranges between 1 and 2 m (Humlum, 2005). ALT data are available from the Global Terrestrial Network for Permafrost (GTNP) database (http://gtnpdatabase.org/) for several locations on Svalbard, but for different time periods and distances between 25 and 115 km away from Bayelva. The site with the longest record, Janssonhaugen, is located 115 km to the southeast and had an average thaw depth of 175 cm for 1998–2013. The region has experienced increases in cloudiness, precipitation, and the number and intensity of cyclones in recent years, especially during the winter months (Hanssen-Bauer and Førland, 1998; Sepp and Jaagus, 2011). The increase in cloudiness (Maturilli and Kayser, 2016) has led to an increase in incoming long-wavelength radiation,

resulting in a major change to the winter radiation budget for this region, as measured at the German-French (AWIPEV) research station, which is located within the village of Ny-Ålesund (Maturilli et al., 2014). This research station carries out long term monitoring of radiation (Baseline Surface Radiation Network: http://bsrn.awi.de/) and meteorological data (http://www.awipev.eu/).

The data presented herein were collected from the High Arctic Bayelva River catchment area (Figure 1), away from Ny-Ålesund. A legacy from past mining activities is the physical disturbance of the ground in and around Ny-Ålesund (for example, compaction and reworking of the soil). Traffic in the village (people, cars, snow mobiles) also affects the surface conditions, especially in winter. The Bayelva catchment area lies between two mountains (Zeppelinfjellet and Scheteligfjellet), with the glacial Bayelva River originating from the two branches of the Brøggerbreen glacier. The terrain flattens out to the north of the Bayelva site and the Bayelva River flows into the Kongsfjorden fjord and the Arctic Ocean about 1 km from the site (Figure 1). Over the past three decades the Bayelva catchment area has been the focus of intensive investigations into fluvial hydrology (sediment transfer and geochemistry; (Hodson et al., 2002)), soil and permafrost conditions (Boike et al., 2008b; Roth and Boike, 2001; Westermann, 2010; Westermann et al., 2011b), the surface energy balance (Boike et al., 2003b; Westermann et al., 2009), and the micrometeorological processes controlling the surface gas and energy exchanges (Lloyd, 2001b; Lloyd et al., 2001; Lüers et al., 2014). A permafrost maximum, minimum and average temperature with depth (trumpet curve) was shown for data for one year (August 2009–August 2010) by Boike et al., (2012).The data from this Bayelva site have also been used in earth system modeling (Ekici et al., 2014; Ekici et al., 2015). Nearby investigations by Japanese and Italian researchers include vegetation analysis with respect to periglacial and glacial landforms and topography (Cannone et al.,

2004; Ohtsuka et al., 2006), and investigations into the plant and plot scale dependence of CO_2 emissions on biotic and abiotic factors at the start and end of the growing season (Cannone et al., 2016; Uchida et al., 2006).

The Bayelva site is located on top of the Leirhaugen hill (25 m a.s.l.), on permafrost patterned ground (Figure 2). The hill consists mainly of rock but is partly covered by a mixture of sediments that consist of glacial till, together with fine grained glacio-fluvial sediments and clays from the last glacial advance, likely deposited by the Kongsfjorden glacier (J. Tolgensbakk, personal information). According to the geological map, the site is part of the Brøggerbreen Formation (lithography sand-stone, shale, conglomerate), but the gray color of the sediments suggests that the material was deposited by the Kongsfjorden glacier and not the adjacent Brøggerbreen glacier, which deposits redder material. Thus, the site is part of the Kongsfjorden Formation, with the main lithography sandstone, shale, coal (Norwegian Polar Institute online geological maps, accessed December 2017). ~~The gray color of these sediments suggests that they derived from the Kongsfjorden glacier and not the adjacent Brøggerbreen glacier, whose sediments have a more reddish color.~~ Since the hill has a maximum altitude of about 38 m, which is below the ~~maximum height for marine sedimentation~~upper marine limit, these sediments may also include marine deposits.

The vegetation cover in the vicinity of the Bayelva site (i.e. the area of the hill) has been estimated to be approximately 50-60 %, with the remainder being bare soil with a small proportion of stones (cobbles and gravel) (Lloyd et al., 2001). Within the rest of the Bayelva River catchment area, sparse vegetation alternates with bare soil and sand, or with rock fields.

The area of the Bayelva site is covered with non-sorted circles, also known as mudboils (Figure 2), which are only present on the hill itself, with other patterned ground phenomena

(such as sorted circles and stripes) occurring on and in the area surrounding Leirhaugen hill. These non-sorted circles formed under localised favourable conditions following the last glacial period. The bare soil centers of these circles are about 1 m in diameter, surrounded by a vegetated rim that consists of a mixture of low vascular plants (including various species of grass and sedge such as Carex spp., Deschampsia spp., Eriophorum spp., Festuca spp., and Luzula spp.), catchfly, saxifrage, willow, various other locally common species (Dryas octopetala, Oxyria digyna, Polygonum viviparum), and some unclassified species of moss and lichen (Ohtsuka et al., 2006; Uchida et al., 2006).

The soils on the hill generally range from "silty loam" to silty clay" with a few large stones. The silt content decreases from more than 50 % at the top of the soil profile to less than 30 % at the bottom of the soil profile at about 1 meter depth, while the clay content increases to more than 50 %. Concentrations of total organic carbon, total nitrogen, and total sulphur are highest at the bottom of the soil profile, peaking below the centers of the non-sorted circles. The organic carbon concentration is high (> 6 % weight) at the bottom of the soil profile. Nitrogen is elevated beneath the vegetated rim of the non-sorted circles (Boike et al., 2008a).

The Bayelva site can be temporarily shaded from direct solar radiation by the mountains on either side. Snow is present for up to 9 months of the year and strong winds can encourage drifting and snow redistribution. The snow depth ~~of the snow cover~~ varies within the Bayelva catchment area, as do its physical characteristics, such as the snow-water-equivalent and the internal stratigraphy and density of the snow pack. A 15 m x 10 m fence surrounds the Bayelva site to prevent reindeer from damaging the equipment, and a small wooden container (about 0.90 m x 1.40 m, and 2.3 m high) houses the data acquisition and transfer system (Figure 2). Warm weather events during the winter can interrupt the build-up of snow cover

resulting in the formation of either internal ice lenses or basal ice, depending on the heat content of the snow pack. Table 1 summarizes the characteristics of the site retrieved from both previous publications and data included in this paper.

3 Data description

The Bayelva site was powered by a solar panel and wind generator during the period from 1998 to 2013 and data retrieved manually through site visits every 4 to 6 weeks, when visual inspections were made of the sensors.

Since 2013 the site has been connected to the mains electricity supply and the Ny-Ålesund data network, and data has since then been transferred automatically resulting in much improved data collection with almost no data gaps. The data gaps prior to 2013 resulted mainly from problems with the energy supply for the site, such as problems with the solar/wind charge regulator. The current online data transfer and real time data visualization enables real time data checking and identification of possible sensor failure, as well as remote programming. Major problems that have affected the continuous data collection or the data quality include reindeer disturbance (e.g. reindeer pulling cables out of the ground, or destroying sensors by rubbing against the stations, as occurred in 2003) and the gradual uplift of sensors as a result of freeze-thaw processes, which affected soil temperature measurements.

Details of the sensors are provided in the following sections, as well as descriptions of the data quality and cleaning routine (Section 4). The instruments are divided into above-ground (meteorological) and below-ground sensors (for example, soil sensors). Further detailed information on the sensors can be found in Table 2, which summarizes all of the parameters and instruments (Table 2), as well as in Appendix C and Appendix D (metadata and

description of instruments). Figure 3 presents time series of parameters between 1998 and 2017.

3.1 Weather station data

Meteorological data have been recorded at the AWIPEV Research Base in Ny-Ålesund since 1992, including radiation component data for the worldwide Baseline Surface Radiation Network (BSRN). The AWIPEV meteorological data are described by (Maturilli et al., 2013) and can be downloaded from PANGAEA (http://bsrn.awi.de/data/data-retrieval-via-pangaea/). Climate records covering a longer period of time ~~(since 1989)~~ are available from ~~the airport in Longyearbyen, which is about 110 km from Ny-Ålesund (Nordli et al., 2014)~~ Svalbard since 1898, with the establishment of a permanent weather station in 1911 (Førland et al., 2011).

Since the Bayelva site is located close to the leading edge of the Brøggerbreen glacier, a different local micro-climate can be expected from Ny-Ålesund. A climate station was therefore installed in 1998, within the fenced area. The temporal resolution of the meteorological measurements was increased in October 2009, from 60 minutes to 30 minutes.

3.1.1 Air temperature, relative humidity, and snow temperature

Air temperature and relative humidity (hourly averages, since 2009 half hourly averages) are measured at a height of 2 m above the ground surface using PT100 platinum resistance temperature sensors and Rotronic MP103A/Vaisala HMP45 capacity sensors, protected by unventilated shields. The heights of the shields are not adjusted during periods of snow cover accumulation or ablation. The uncertainty in the temperature measurements ranges between

0.03 and 0.5 °C, depending on the sensors used; the uncertainty in the relative humidity measurements ranges between 2 and 3%. The PT100 temperature sensors were calibrated in ice-slush water for at least 12 hours to determine the absolute accuracy at 0 °C. The precision of the temperature sensors was calculated from the variation in values recorded during the calibration period, at constant temperatures in ice-slush water, and can be found in Table 2.

The change of sensors for relative humidity in 2009 resulted in 7 percentage points lower average relative humidity between 2009 and 2017 as compared to the period before, independent of the season.

Snow temperature

PT100 temperatures sensors were installed at the weather station in 1998, close to the ground surface. When covered by snow these sensors record the snow temperature, while during the snow-free period they record (unshielded) air temperatures. The temperature cables were originally attached to a small (vertical) bamboo stick, with sensors sticking out a few cm from the stick (Appendix C, ~~fig.~~Figure C5). Visual inspections during late spring (May 2016) revealed that melting occurred around the bamboo stick, leaving an air gap around the stick. The temperature sensors were nevertheless well away from the stick (in a horizontal direction) and remained embedded in the snow. The height of the sensors was changed on a number of occasions following damage by reindeer. Sensors were originally mounted at heights of 0.35 and 0.48 m to record snow temperatures, but these heights were changed during subsequent years (Table 2). Information concerning the changes in sensor height is included in the data description that accompanies the data (Appendix C, ~~fig.~~Figure C5).

3.1.2 Wind speed and direction

The wind speed and direction were measured with a R.M. Young propeller anemometer (Model 05103). The wind direction, its standard deviation was recorded at hourly (1998-2009) or half-hourly (2009-present) intervals.

3.1.3 Radiation

Net radiation was first measured in 1998 using a CSI (Campbell Scientific Ltd.) Q7 net radiometer, which was replaced in 2000, reinstalled between May 2002-Sept 2003 with an NR Lite net radiometer (Kipp & Zonen) and in 2009 with a NR01 four-component sensor (Hukseflux). A wind correction was performed according to the manufacturer's suggestion for the Q7 and NRLite net radiometers (Campbell Scientific Ltd.; details in Appendix C & D). An SP 1110 (Skye Instruments) pyranometer was also installed in 1998 and a CG1 (Kipp and Zonen, Appendix C3) downward-looking pyrgeometer (to detect reflected longwave radiation) in 2003. Regular site visits were made during which the pyranometers were checked for condensation, dirt, physical damage, or hoar frost. Nevertheless, because the instruments were largely unattended most of the time, we estimate the field accuracy to have been between ±10 % (for the Q7 sensor) and ±20 % (for the NR Lite). The Q7 sensor was destroyed by reindeer in September 2003 and was not replaced. The fence was improved in 2017. Details on the various net radiometer set ups and correction are provided in Appendix D.

3.1.4 Rainfall

An un-heated and un-shielded tipping bucket rain gauge (R M Young, 52203) was installed on a pole in August 1999, with the top of the bucket about 1.6 m above ground ~~L~~level. The instrument measures only liquid precipitation (rainfall) and not winter snowfall. The tipping bucket was regularly checked in summer by pouring a known volume of water into the bucket and by frequent visual inspections for dirt or snow during each site visit. At wind speeds above 12.5 m/s (hourly or half hourly average) the rain gauge was found to record precipitation even when there was none, due to vigorous shaking of the pole; these data were flagged accordingly within the data series. Until 2010, precipitation was only recorded as hourly totals, but the provided data set uses 30 minute temporal resolution (half hours are presented as "NaN", since the hourly total is given at full hour). Total daily precipitation figures from a gauge in Ny-Ålesund are available through the The Norwegian Meteorological Institute (formerly: www.eklim.no, www.met.en).

3.1.5 Snow depth

The snow depth around the station has been continuously monitored since 1998 with an SR50 sonic ranging sensor (Campbell Scientific Ltd.) and with an additional SR50 sensor at a nearby (about 85 m away; Figure 2) eddy station since 2006. The sensor recorded raw distance data from the sensor to the object (in this case the ground or snow surface). The data obtained from the sonic sensor was corrected using the speed of sound at 0 °C and the air temperature measured at the Bayelva site, using the formula provided by the manufacturer (Campbell Scientific Ltd.; Appendix D, D4). To obtain the snow depth the distance of the sensor from the ground surface was recorded annually and subtracted from the corrected

distance data. Snow depths are provided in the data supplement for this paper. Due to seasonal thawing of the ground, the surface can subside over the season (Overduin and Kane, 2006), thus negative distance rates of a few cms are computed (and not set to zero). The data are not removed from the series since the opposite process, frost heave, takes place during fall freeze back and thus the surface bounces back to the original height. Since the ground surface has little or no vegetation cover the signal is returned with a high degree of accuracy (Table 2). An additional snow depth laser distance sensor (Jenoptik SHM30) was installed at the Bayelva site climate tower in August 2013. The data from the three different snow depth sensors was combined to obtain a continuous record and fill any gaps left by the failure of individual instruments ("Level 2 data" containing all original snow data from the three sites "merged" into one data product, can be found in Section 4). ~~It should be noted that two of the sensors (an SR50 sensor and the laser sensor) were located within 5 m of each other, while the second SR50 (at the eddy covariance site) was located 85 m away, downhill from the Bayelva site (Figure 2).~~ Any differences in snow depth between these sensors may therefore be due to microtopographic and microclimatic variations between these two locations.

3.1.6 Time lapse photography of snow cover

In order to monitor the timing and pattern of snow ~~melt~~ cover changes an automated camera system (K1; UIT) was set up in August 2013 to photograph the land surface in those areas in which the instruments were located (Figure C2). The camera recorded one image every hour; during the polar night a light was switched on automatically while each image was being recorded.

3.1.7 Dielectric number of snow

The dielectric number of the snow was measured using a vertically installed time-domain reflectometry (TDR) probe. The length of the TDR probe was 0.5 m between 1998 and 2007 and 0.33 m from 2009 onwards. Dielectric numbers are provided in the data set for both the snow-covered and the snow-free periods (recording only air dielectric numbers). When the snow cover depth exceeds the length of the TDR probe the dielectric number data can be used to infer dry snow densities using empirical relationships (Schneebeli et al., 1998). In wet snow, the measured snow dielectric number can be used for the calculation of the snow liquid water content using the composite approach with ice added as an additional phase (for example, Roth et al., 1990) and measured snow densities (Appendix E, table. E1).

3.1.8 Vertical profiling of the physical properties of snow

Snow depth, together with vertical profiles for temperature, density, and dielectric numbers were collected from the site and surrounding areas during a number of end-of-snow (spring) seasons. These profiles, which were collected at irregular intervals between 2000 and 2016, provide additional information on the snowpack. They typically reveal the presence of a number of ice layers (including a basal ice layer) and snow densities of between 220 and 440 kg/m^3. The typical end-of-spring average snow density before snow melts is 350 kg/m^3. The end of spring season snow-water-equivalent varies between the years due to variations in snow depth (Figure 4). Details of these profiles, including some stratigraphic information, are provided in Appendix E (Table E1).

3.2 Subsurface data on permafrost and the active layer

Data have been collected from a variety of installations that were changed over time because of the deterioration of sensors or disturbance by reindeer. As a result, there are a number of data series from different profiles rather than one continuous data series. Some measurements were also discontinued (for example, soil heat flux).

3.2.1 Instrument installation and soil sampling

In order to take into account any possible effects of small variations in vegetation and microtopography at the site (e.g. due to the presence of non-sorted circles), instruments were installed in a number of different positions within a profile. Deterioration of data quality and the failure of some sensors also led to the installation of new sensors in new profiles.

Instrument installation and soil sampling 1998

The first set of instruments was installed in 1998, within one of the non-sorted circles (Appendix C, Figure C7), for which a trench 2 m wide and 1.4 m deep was excavated across the circular feature (Appendix C, Figure C8). The surface was carefully cut and the excavated soil stockpiled separately according to depth and soil horizon, in order to be able to restore the original profile following installation of the instruments. The unfrozen layer was 1.2 m deep at the time of installation. The entire profile was quite heterogeneous but consisted mainly of silty clay, with a stone content of less than 10 %. The stone content increased to about 50 % in a slightly inclined layer approximately 20 cm thick that occurred at a depth of 50 cm; the stones were quite large (including cobbles in excess of 6 cm in diameter) but showed no preferred orientation. Below 85 cm depth the soil was coal-rich and contained massive coal lenses.

Sensors were installed horizontally and vertically in the undisturbed wall of the trench profile (Appendix C Figure C8b) to obtain a 2 D profile instrumentation, which was then backfilled. Soil samples were collected during the installation so that physical parameters could be analyzed. The stratigraphic and textural information from the soil profile, including soil organic carbon (C), nitrogen (N) and sulfur (S) concentrations, can be found in Appendix F.

Soil sampling 2007

A number of additional soil profiles in the vicinity of the Bayelva site were sampled in 2007 (Figure 2). Data for the soil texture, bulk density and carbon, nitrogen and sulphur (C, N, S) content of these profiles is also included in Appendix F (Table F1).

Instrument installation and soil sampling 2009

A new set of measurement profiles was established within a second non-sorted circle close to the 1998 profiles (Appendix C, Figures. C9). The site was chosen for its similarity to the 1998 site, in order to provide an analogous continuation of the long term subsurface data from the 1998 profiles. Data on the soil texture, its bulk density, and carbon, nitrogen and sulphur content can be found in Appendix F.

All profiles show cryoturbation features at the surface through patterned ground (non-sorted circles) and also within the soil profile, for example, roots that are transported downwards through cryoturbation (Figures C8 & C9).

3.2.2 Ground temperature

Soil profile sensor installation, 1998

Pairs of soil temperature and soil water content sensors were installed over a vertical 2D profile in 1998; their positions are shown in Appendix C (Figures –C7 & C8). The probes automatically recorded temperatures from that time until January 2012. The temperatures were measured using CSI (Campbell Scientific Ltd.) thermistors connected to a CR10X datalogger with an AM416 multiplexer. The voltage measured for each sensor was stored in a database. Temperatures were calculated from the raw data using the Steinhart-Hart equation (Steinhart and Hart, 1968) and sensor calibration at 0 °C (Table D2). The average accuracy determined through calibration was 0.01 °C with a precision better than 0.002 °C. However, the max deviation at 0 °C was 0.1 °C. After installation, the sensors cannot be re-calibrated, certainly not without a lasting physical disturbance of the profile. However, temperatures during spring thaw and fall refreezing are stable at the phase change temperature (the zero-curtain effect in permafrost soils). Assuming that freezing point depression (i.e. soil type and soil water composition) does not change significantly from year to year, these periods can be used to evaluate sensor stability. During the first two years (1998-1999) the temperatures during these periods were stable to within 0.1 °C. Subsequently, temperature readings from nine of the 32 sensors ~~subsequently~~ started to drift and showed a positive offset relative to the ~0 C zero-curtain period. The temperature sensor at 19 cm depth for example, showed correct temperatures during the fall freeze-back of 1998 and 1999, but in the fall of 2000 the measured soil temperatures shifted to positive values by 0.5 C (offset from the fall zero-curtain). This offset increased further to about 6 C in 2009. All sensors with temperature offsets of 0.5°C or more were flagged accordingly within the data set. The positive temperature offset was most likely due additional resistance, either in the cables due to leakage currents or in the multiplex due to corrosion. In addition to the temperature offset, the data quality of the years 2002 to 2007 was strongly affected by irregular spikes caused by the

multiplexer. In the worst year, 2002, these spikes occurred for 5 to 7% of all measured values in all soil temperature series of the 2D profile. Spikes were flagged automatically and manually within the data set. The external charge controller regulating the solar and wind energy supply was changed in 2002 following a power failure, resulting in increased noise ~~L~~levels in the measured temperatures between 2002 and 2012 and subsequent discontinuation of this data series.

Soil profile sensor installation, 1999

Temperature sensors were installed in 1999 in one additional vertical profile, 2 m apart, within the fenced off area, below vegetation (b in Appendix C, Figure C6). A small-diameter (vertical) hole was drilled by a hand drill into the ground in the fall of 1999. The PT100 temperature sensors were calibrated in ice-slush water for at least 12 hours to determine the offset at 0°C. The max deviation at 0°C was 0.1°C. Similar to the 107 probes, the average accuracy determined through calibration was 0.01°C with a precision better than 0.002°C. Wooden sticks to which sensors had been attached were then inserted into the holes down to 1.50 m into the ~~permanently frozen soil~~permafrost beneath the active layer in such a way that the sensors formed a tight fit in the hole and no air was able to pass. The temperature sensors were attached at regular intervals to bamboo sticks. The upper sensors were affected on September 11, 2003 by reindeer disturbance. Furthermore, the upper two sensors moved upwards by about 10 cm between 2003 and 2016 due to frost heave and they were removed from the data series.

Soil profile sensor installation, 2009

Pairs of soil temperature (CS107) and water content (TDR) probes were installed during August 2009, close to the first profile, that was installed in 1998 (Appendix C, Figure C9). Soil temperatures were measured at 11 depths in a profile from the surface down to a depth of 1.4 m. The data quality from the 2009 system improved considerably to the 1998 system, probably due to the data logging and multiplexer system used (CR10X from 1998 to 2011; CR1000 since 2009). Data collection is ongoing.

3.2.3 Soil dielectric number, volumetric liquid water content, and bulk electrical conductivity

Soil profile sensor installations 1998 and 2009

Time-domain reflectometry (TDR) probes ~~were installed~~ were installed in horizontally adjacent to the temperature probes installed in soil profiles in 1998 and 2009 (see above and Appendix C (Table C5).

These TDR probes automatically recorded hourly measurements of bulk electric conductivity and the dielectric number, obtained by measuring the amplitude at very long times and the L_a/L ratio (ratio of the apparent to real probe length, corresponding to the square root of the dielectric number). From 1998 to 2008 the measurements were obtained using a Tektronix 1502B cable tester connected to a CR10X data logger and custom made triple wire 24 cm probes. Since 2009 a CSI TDR100 reflectometer has been used, connected to a CR1000 datalogger and 30 cm TDR CS605 probes (Campbell Scientific Ltd.). All TDR probes were calibrated for probe offset following the method described in (Heimovaara and de Water, 1993) and the CSI TDR 100 manual (http://www.campbellsci.de/tdr100). The dielectric number data and computed volumetric liquid water in frozen and unfrozen soil are provided

with the data set. The calculation for volumetric liquid water content takes into account four phases of the soil medium (air, water, ice, mineral) and uses the mixing model from Roth et al. (1990; Appendix D, D1).

Time-domain reflectometry can also be used to measure the impedance Z (Ω) of the bulk soil, which is related to the soil's bulk electrical conductivity (BEC). These data were used to infer the electrical conductivity of soil water and solute transport in the non-sorted circle over a period of one year (Boike et al., 2008a). The impedance can be determined from the attenuation of the electromagnetic wave traveling along the TDR probe after all multiple reflections have ceased and the signal stabilized. The bulk electronic conductivities were recorded hourly using the TDR setup described in this section. The equipment installed in 1998 was calibrated in pure water, in air, and in NaCl solutions with various known conductivities, and is corrected for temperature (25°C), following the method by (Heimovaara et al., 1995). The TDR equipment installed in 2009 was not calibrated for BEC and a probe constant of 1 was used for BEC waveform retrieval; Campbell Scientific Ltd. suggests a probe constant (K_p) for the CS605 probes of 1.74. The lack of calibration explains the differences of the data sets recorded between the time 1998-2009 and 2009 to present (Figure 3i). Measurements of electric conductivity and the dielectric number were affected by irregular spikes and possibly by sensor drift similarly to the soil temperature measurements. Spikes were flagged automatically and manually, while drifts could not be flagged due to the lack of reference data. Overall, the quality of soil data instrumented in 1998 is of reduced quality since July 2005. Values for dielectric number, computed volumetric liquid water content, and bulk soil electrical conductivity can be found in the data set.

3.2.4 Soil heat flux

Two heat flux plates (Hukseflux HFP01), one installed at 0.18 m depth below the unvegetated center of the non-sorted circle and the second at 0.24 m depth below the vegetated rim of the non-sorted circle, recorded ground heat flux between September 1998 and September 2009 (Figure 3). The manufacturer's calibration values were used to record heat flux in W m^{-2}.

3.2.5 Permafrost and active layer temperature

A 9.3 m borehole was drilled using a rotary drill rig on March 30, 2009 and cased with PVC. No stratigraphic information or drill core was recovered. ~~Ten thermometers were~~ A thermistor string was installed, with one sensor above the ground surface and nine from the surface down to 9 m depth (at 0, 0.5, 1.0, 1.5, 2.5, 3.5, 5.5, 7.5, 9 m below ground surface, Appendix C, Figure C10). The casing was left open (not refilled) so that the ~~thermometer~~thermistor chain could be retrieved or replaced. Because of instrument failure, thermometers were retrieved and replaced several times. From August 2009, a Geoprecision-M datalogger and sensor chain were used. Temperatures were recorded at hourly intervals, with no averaging; no data was recorded between 30 January 2011 and 29 March 2011, due to a low battery voltage. Geoprecision claims an accuracy of +/-0.05 C (at 0°C) and a resolution of 0.01°C, suitable for measurements in the range from -50 to +120°C. However, comparison measurements using an PT100 thermometer at the same depths in the borehole showed a deviation of up to 0.2°C. In 2014, a wooden shield was installed over the casing to prevent warming due to radiation and to facilitate natural ventilation (Appendix C, ~~f~~Figure C10). ~~It is recommended that the temperature data from sensors installed above ground and down to a depth of 1.5 m should be used with caution because of air exchange within the casing.~~ Caution is warranted when using

the borehole temperatures in the uppermost 1–2 m, since they may be affected by air movement in the borehole. These data are flagged in the data series.

4 Data quality control and availability

The primary purpose of quality control of observational data is to detect missing data, errors in the data, and possibly to correct errors in order to ensure the highest possible standard of accuracy and optimal use of the data by the broadest range of possible users. We differentiate between different data ~~L~~levels, from online data (http://www.awi.de/im-fokus/permafrost/direkter-draht-in-den-permafrost.html) to Level 2 data (Table 3). Data supplied with this paper are Level 1 and Level 2 data. Level 1 data have undergone an extensive quality-control and are flagged with regards to maintenance periods, physical plausibility, spike/constant value detection, sensor drifts (Table 3). Level 2 data are compiled for special purposes such as a combination of data series from multiple sensors and gap-filling of data (documentation of source data is supplied in the PANGAEA data archive). Examples in this paper of Level 2 data are the snow cover, soil temperature, and soil volumetric water content data series that have been combined from various stations into a single data series, in order to obtain a long term picture. There are 8 quality control types (Table 3). These flags include information on the system's maintenance, no data availability, system error, as well as on consistency checks based on physical limits, gradients, and plausibility. Due to the failure of some sensors that cannot be retrieved for repair or re-calibration (for example, sensors installed in the ground), the initial accuracy and precision of the sensors is not maintained.

In the case of soil temperature, the accuracy can be estimated by analysis of temperatures relative to the fall zero-curtain effect assuming soil water composition is similar from year to

year. As an example, our temperature data have been checked through the fall zero-curtain effect and thus provide information on any reduction in accuracy (see Table 3, Flag 7). These checks are mandatory when small warming trends are to be estimated and interpreted. The selection of flagged data depends on its application and the required accuracies.

The data from this Bayelva site have been widely used for the development and evaluation of land surface models (e.g. Chadburn et al., 2017; Chadburn et al., 2015; Ekici et al., 2014; Ekici et al., 2015). The newly collated dataset will allow multi-year model runs, with improved quality control and checks. The dataset presented herein is freely available, either as download from PANGAEA (https://doi.org/10.1594/PANGAEA.880120) or from the supplementary material of this paper. The data are provided as ASCII files. Other available data sets include a flux data set in the European Fluxnet Database (Lüers and Boike, 2013) and aerial imagery of the snow cover (Westermann et al., 2015). Volumetric soil liquid water content and snow cover data are transferred in real time to the NASA SMAP mission (https://smap.jpl.nasa.gov/) and are uploaded to the PANGAEA archives on an annual basis.

5 Outlook

Permafrost around the Arctic is warming and thawing ~~and warming~~ (Christiansen et al., 2010; Romanovsky et al., 2008), and this is true for Svalbard (Isaksen et al., 2007b) and the Bayelva site as well. The record from 2009–2017 of permafrost temperature measurements shows a zero-amplitude depth of 5.5m, at a mean temperature of -2.8°C. Mean annual, summer and winter soil temperature data at all depths have been ~~warming~~rising over the period of record (Figure 4, three depths are shown) as well as in the deeper permafrost (Figure ~~4~~3h).

Interannual to sub-decadal variability is evident in the data and results mostly from differences during the winter months. Future analysis is required to detangle the relationship between potential meteorological drivers and permafrost degradation at this site. The data set described and distributed in this paper provides a basis for analyzing this relationship at one site and a means of calibrating Earth System Modelling efforts over a long observational period. Developing predictive capacity for permafrost warming will be key to understanding the role of the permafrost feedback in the global climate system.

Acknowledgements: The logistical support provided by the AWIPEV Research Base at Ny-Ålesund is gratefully acknowledged. Field support, including data collection, was also provided by Konstanze Piel, Christian Wille, Steffen Frey, Conrad Kopsch, Günther Stoof and Peter Schreiber. We appreciate the support of Klaus-Dieter Matz and Frank Scholten for the preparation of the GeoTIFF versions of the HRSC-AX data products. The authors acknowledge the financial support provided through the European Union's FP7-ENV PAGE21 project under contract number GA282700. We thank the two anonymous reviewers whose comments helped to improve this manuscript.

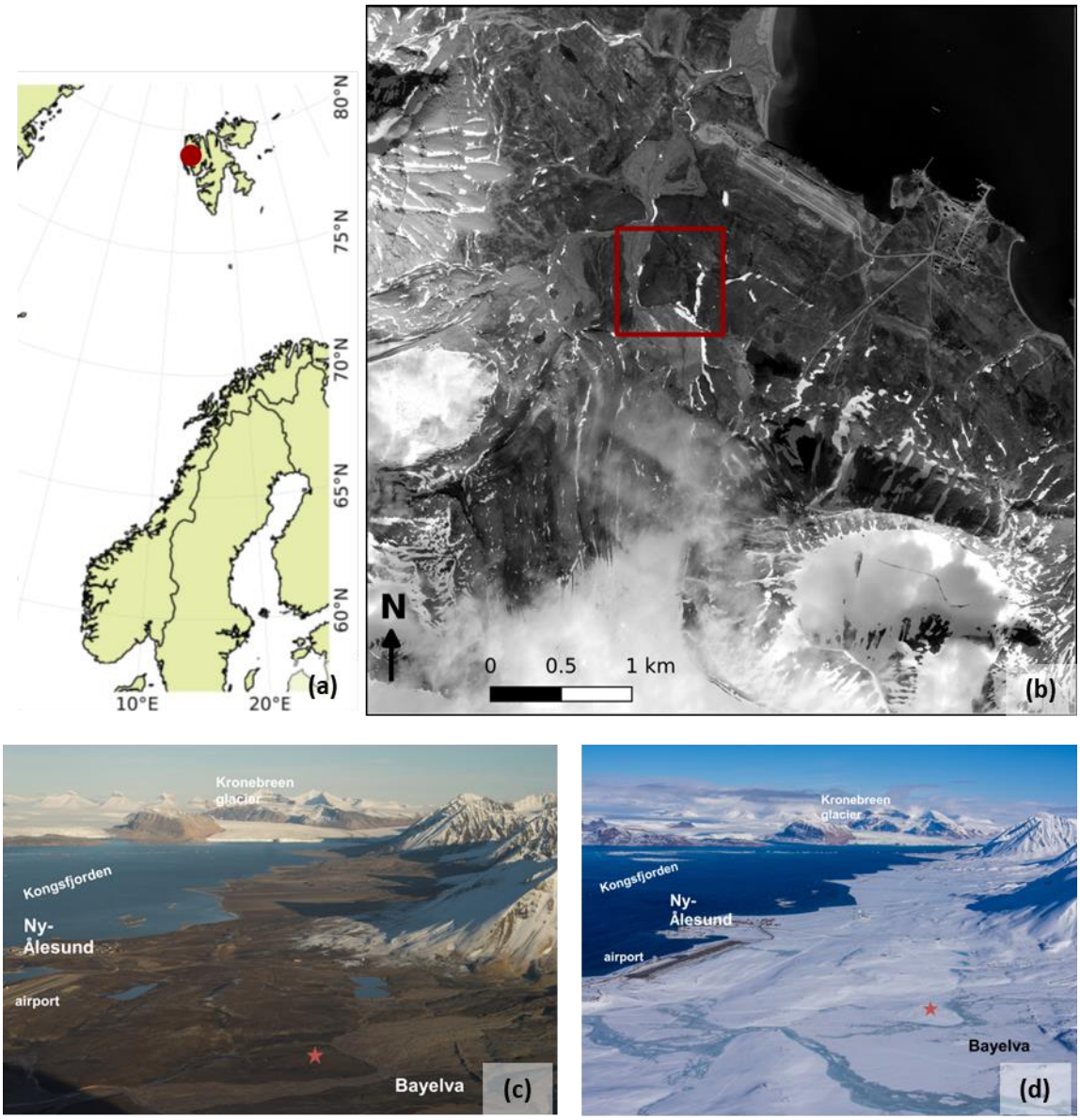

Figure 1. (a) Location of the Bayelva study site on Spitsbergen, western Svalbard at 78°55'15.6"N 11°49'58.5"E. **(b)** The site is located about 3 km from Ny-Ålesund in the Bayelva River catchment area, between two mountains (Zeppelinfjellet and Scheteligfjellet), and in front of the Brøggerbreen glacier. Aerial image captured in August 2008 using a high resolution HRSC-AX camera (Hauber et al., 2011a; Hauber et al., 2011b): data and metadata for the high resolution the HRSC-AX image covering the entire area shown in Figure 1b are provided in Appendix B **(c)** & **(d).** The area of the site under summer conditions (August 2008) and spring conditions (April 2016).

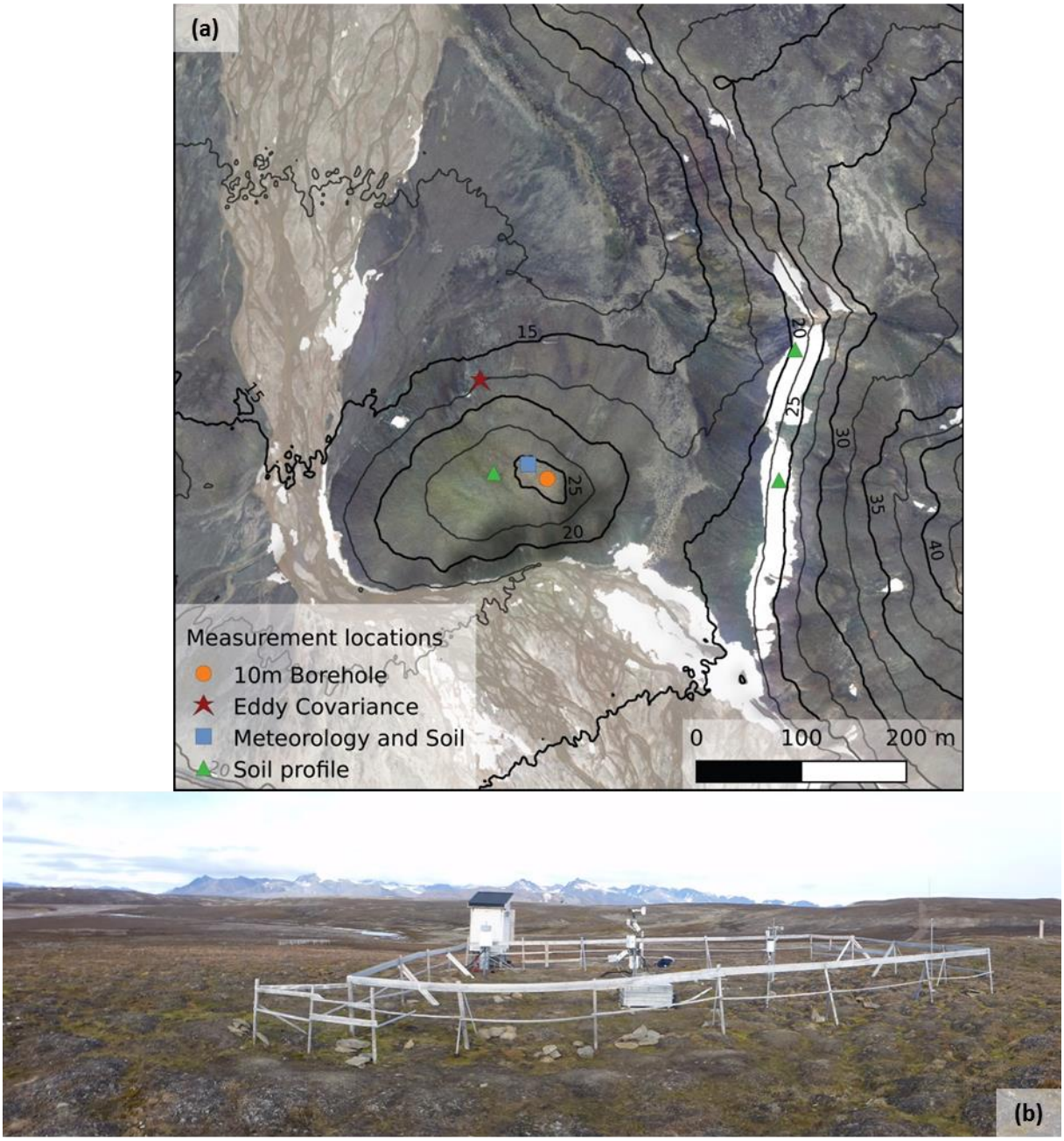

Figure 2. ~~Detailed images of the Bayelva study site on Spitsbergen.~~Topographical map (a) and overview of the Bayelva study site (b) in Ny-Ålesund, Svalbard. **(a)** Aerial orthoimage (20 cm/px) ~~and~~with topographic information (2.5 m contour lines) derived from a ~~correspond-ing~~ Digital Elevation Model (DEM) with a cell size of 0.5 m. The locations of the instrumental and sampling sites are marked by coloured symbols. The site is located on a small hill; white areas are snow fields remaining late in the season. The ~~colour image~~orthophoto and DEM were obtained with an HRSC-AX camera in August 2008 (data and metadata for the

high resolution ~~digital elevation model~~DEM covering the entire area shown in Figure 1b are provided in Appendix B). **(b)** Most of the instruments are within a fenced-off area to protect them from reindeer damage. Note that the eddy covariance station and permafrost borehole are located outside the fenced area.

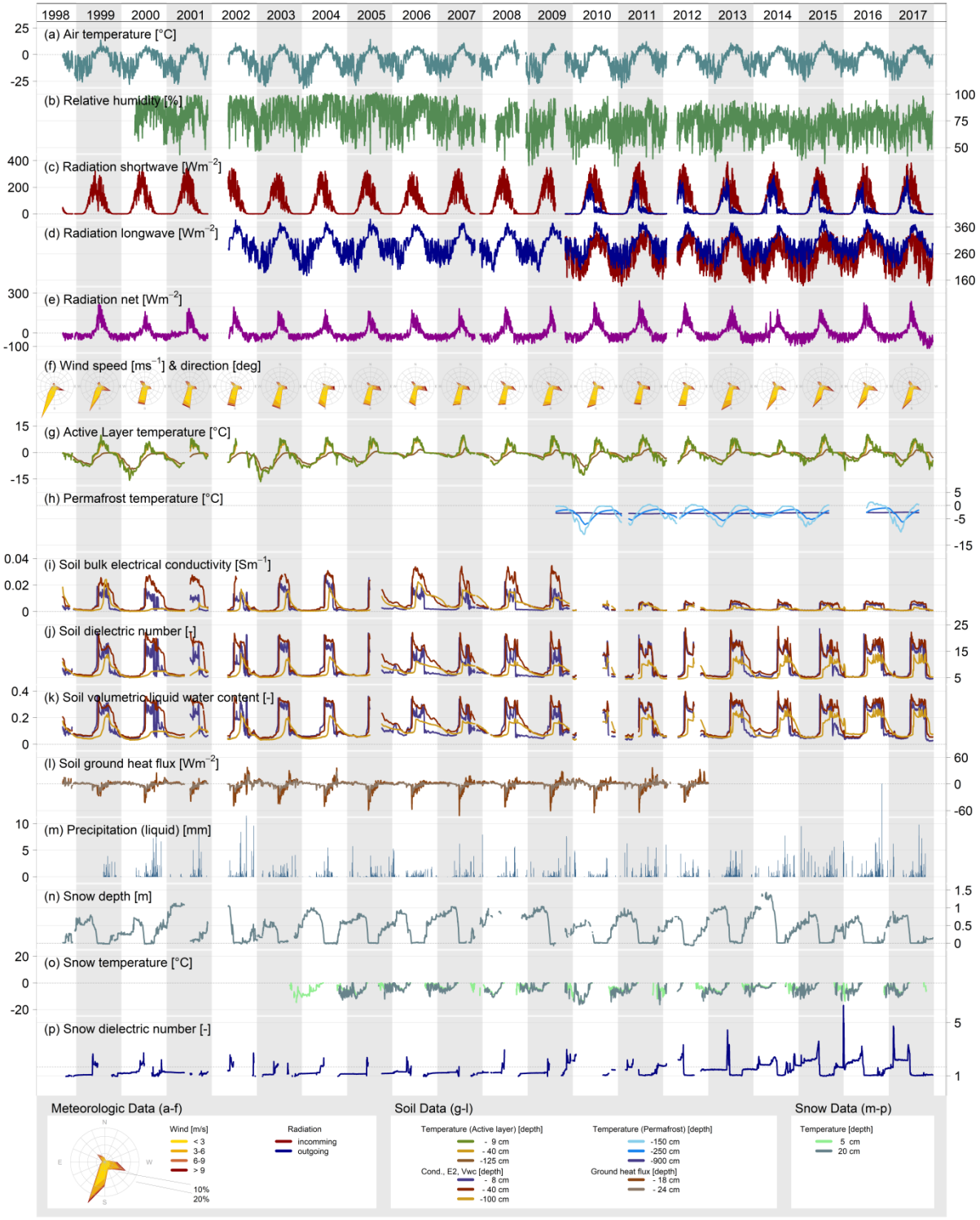
1998 1999 2000 2001 2002 2003 2004 2005 2006 2007 2008 2009 2010 2011 2012 2013 2014 2015 2016 2017
(a) Air temperature [°C]
(b) Relative humidity [%]
(c) Radiation shortwave [Wm-2]
(d) Radiation longwave [Wm-2]
(e) Radiation net [Wm-2]
(f) Wind speed [ms-1] & direction [deg]
(g) Active Layer temperature [°C]
(h) Permafrost temperature [°C]
(i) Soil bulk electrical conductivity [Sm-1]
(j) Soil dielectric number [-]
(k) Soil volumetric liquid water content [-]
(l) Soil ground heat flux [Wm-2]
(m) Precipitation (liquid) [mm]
(n) Snow depth [m]
(o) Snow temperature [°C]
(p) Snow dielectric number [-]
Meteorologic Data (a-f)
Wind [m/s]
< 3
3-6
6-9
> 9
10%
20%
Radiation
incomming
outgoing
Soil Data (g-l)
Temperature (Active layer) [depth]
- 9 cm
- 40 cm
-125 cm
Temperature (Permafrost) [depth]
-150 cm
-250 cm
-900 cm
Cond., E2, Vwc [depth]
- 8 cm
- 40 cm
-100 cm
Ground heat flux [depth]
- 18 cm
- 24 cm
Snow Data (m-p)
Temperature [depth]
5 cm
20 cm

590

Figure 3. Time series of Bayelva data provided in this paper ~~divided into three plots f~~. a-f: meteorological data, g-l: soil/subsurface data, m-p: snow data. The data are organized following the structure of Appendix G. Further details on the sensors and periods of operation are given in Table 2. This plot (divided in three parts for better visibility) is also provided in Appendix H.

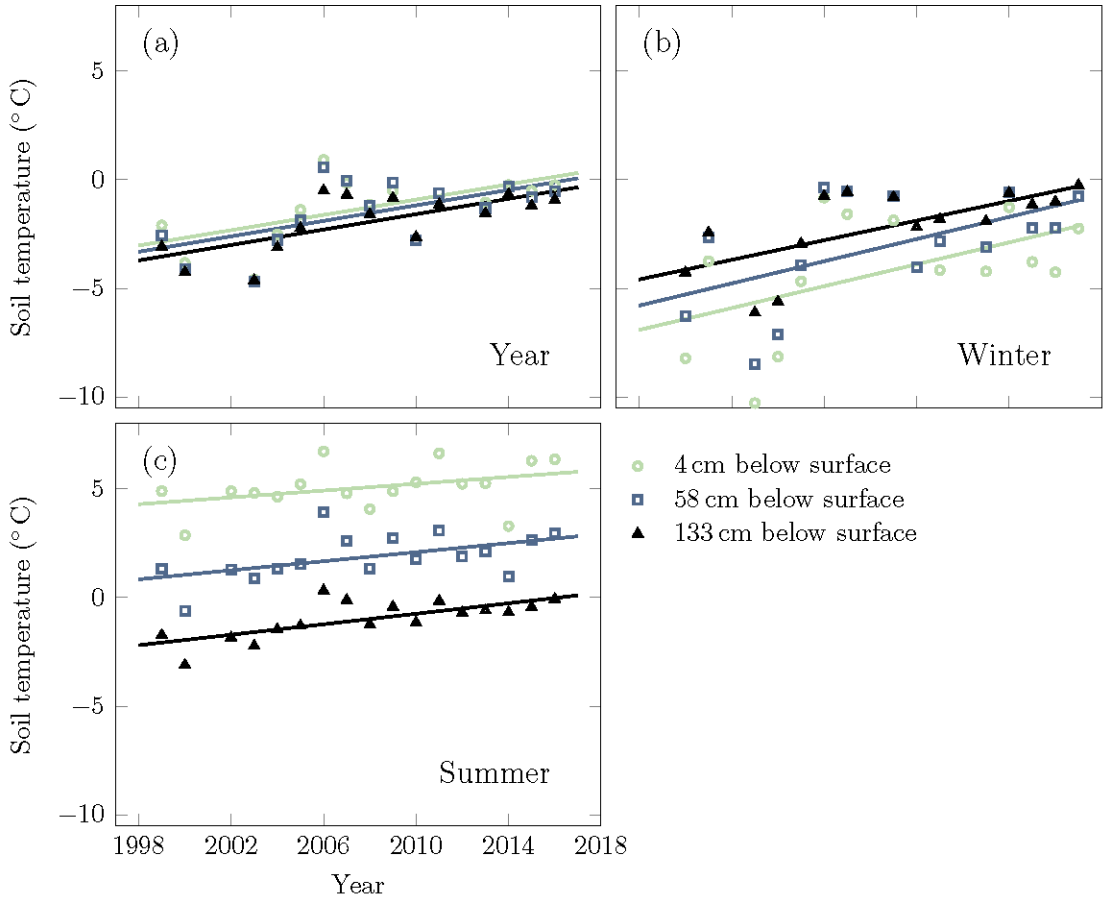

Figure 4. Bayelva mean 20-year ~~soil~~ temperature ~~trends~~ increases for three depths from ~~1998 –~~September 1998 – September 2017 using Level 2 soil temperatures. a) ~~yearly in~~~~trends at all three depths~~ the active layer ~~of~~ (4 and ~~,~~58 cm) and in the top of permafrost (~~,~~138 cm)~~s :~~ ~~are~~ 0.18 ~~°C/year (standard error of trends: ±~~0.07~~, 0.06, 0.05~~ °C/year~~,)~~ b) in winter ~~trends~~ (~~months~~ December, January, February)~~: are~~ 0.25 ±0.12, 0.25 ±0.11, and 0.23 ±0.07°C/year, respectively,~~winter (standard error of trends: ±0.12, 0.11, 0.07 °C/winter)~~ and c) in summer ~~trends~~ (months June, July, August)~~: are~~ 0.08 ±0.05, 0.10 ±0.04, and 0.12 ±0.03°C/~~summer~~ year, respectively. ~~(standard error of trend ± 0.05, 0.04, 0.03 °C/summer).~~ Years in which data gaps of more than 48 hours exceeded 5% of data were included~~:~~. ~~d~~Data gaps were interpolated linearly.

605

Variable	Value	Source
Surface characteristic		
Summer albedo	0.15	Westermann et al. (2009)
Summer Bowen ratio	1 (0.25–2)	Westermann et al. (2009)
Summer roughness length [mm]	1 (by fitting an energy balance model) 7 (eddy covariance)	Westermann (2010)
Snow properties		
Snow albedo	Average for snow covered period prior to melt: 0.81 (2009–2016)	This paper
End of the snow ablation	8 June–11 July	This paper (1999–2016)
Maximum snow depth (end of season before ablation) [m]	range: 0.65–1.42 m average 0.9	This paper (1999–2016)
End of season snow density [kg m^{-3}]	350 ± 50	Westermann et al. (2009) (Boike et al., 2003a)Boike et al. (2003) Appendix E for individual profiles
Snow thermal conductivity [W m^{-1} K^{-1}]	0.34	Computed from snow density of 370 kg m^{-3} using Yen (1981)
Snow thermal conductivity [W m^{-1} K^{-1}]	0.45 ± 0.15	Westermann et al. (2009)
Soil properties		
Organic layer thickness	0–5 cm (bare to vegetated areas; up to 15 cm in wetter areas)	This paper
Thawed soil thermal conductivity [W m^{-1} K^{-1}]	1.3 ± 0.4 at volumetric soil liquid water content 20%–40% (soil profile 1998: profile average)	Westermann et al. (2009)
Soil heat capacity thawed [10^6 J K^{-1} m^{-3}]	2.3 ± 0.5 at volumetric liquidwater content 20%–40%	Westermann et al. (2009)
Frozen soil thermal conductivity [W m^{-1} K^{-1}]	2.0–2.5	Westermann et al. 2011(Westermann et al., 2011a) based on thermal diffusivity provided by Roth and Boike (2001)
Soil texture	Silty clay to sandy silt, , stone content < 10% at surface with up to 50%	Boike et al., 2008a Appendix F for individual pedons

Variable	Value	Source
Soil bulk density [kg m^{-3}]	Average: 1.9 x 10^3 kg m^{-3}	Boike et al. (2008a) Roth and Boike (2001) Appendix F for individual pedons
Soil carbon density [kg C m^{-3}]	6 kg m^{-3} (down to 78 cm) 0–60 kg m^{-3} (range) 2–22 kg m^{-3} (range over averaged vertical profile)	Chadburn et al. (2017) Appendix F for individual pedons
Organic carbon stock [kg C m^{-2}]	4.3 (range: 1.1–7.9 kg C m^{-2} for 0–100 cm	Area between flood plain and sea (Yoshitake et al., 2011). Appendix F for individual pedons
Saturated hydraulic conductivity [m s^{-1}]	10.9 x 10^{-6} 7.11 x 10^{-6}	Weismüller et al. (2011) Ekici et al. (2015)
Clapp-Hornberger exponent (b factor)	5 (for silty loam soil)	Chadburn et al. (2015)
porosity (volumetric water content at saturation)	0.36–0.5	Roth and Boike (2001) Weissmüller et al., 2005
Van Genuchten Parameters: Alpha [1 mm^{-1}]	Alpha = 0.002	Weismüller et al. (2011)
Van Genuchten Parameters: n [unit-free]	1.2–1.5	Weismüller et al. (2011)
Vegetation characteristics		
Vegetation height	0–20 cm (bare soil to vegetated areas)	This paper
Vegetation fractional coverage	50–60 area %, vascular plants cover up to 30%	This paper Lloyd (2001a)
Vegetation type	"Lichen heath" "High Arctic tundra in mesic–xeric conditions" "A mixed community of bryophytes (e.g., Sanionia uncinata, Aulacomnium turgidum and Dicranoweissia sp.) and vascular plants (e.g. Salix polaris, Saxifraga oppositifolia, Oxyria digyna and Dryas octopetala) covered the well developed vegetation among topograph-	Brattbakk (1981) Cannone et al. (2004) Uchida et al. (2009)

Variable	Value	Source
	ical undulation."	
Leaf Area Index (LAI)	0 (no vegetation areas) 0.3–0.7	Cannone et al. (2016)
Root depth	~19 cm	This paper
Leaf dry biomass	26–195 g m^{-2} for small patches of 100% vegetation cover of three different species	Muraoka et al. (2008)
Landscape		
Landscape type	Glacial outwash flood plain	This paper
Bioclimate subzones	Subzones A and B, characterized by barren ground and scattered vegetation. The vegetation mainly consists of non-vascular plants (40% cover) and a few vascular plants (5% cover). The average total phytomass in this subzone is lower than 3 t ha^{-1} and the net annual production is lower than 0.3 t ha^{-1}.	CAVM-Team (2005)

Table 1. Site description parameter for earth system model input. Values have been computed and compiled for the Bayelva site and surrounding areas.

610

Variable	Sensor	Period of operation from	to	Height [m]	Unit	Measuring interval	Integration method	Spectral range	(Field) accuracy [±]
Meteorological sensors									
Air temperature	Rotronic MP103A	Apr 2000	Aug 2009	2	°C	20 s	avg[1] 1 h		0.5 °C (at -40 °C to +60 °C)
Air temperature	Vaisala HMP45	Aug 2009	…	2	°C	60 s	avg 30 min		0.2 °C (at 20 °C)
Air temperature	1x PT100	Aug 1999	Aug 2009	8/1999[2]: 2 4/2000: 1	°C	15 min	avg 1 h		0.03 °C
Air temperature	1x PT100	Aug 2009	…	1	°C	60 s	avg 30 min		0.03 °C
Relative humidity	Rotronic MP103A	Apr 2000	Aug 2009	2	%	20 s	avg 1 h		3 % (at 20 °C)
Relative humidity	Vaisala HMP45	Aug 2009	…	2	%	60 s	avg 30 min		2 % (at 20 °C, 0 to 90 % RH); 3 % (at 20 °C, 90 to 100 % RH)
Wind direction	R.M. Young anemometer 05103	Sep 1998	Aug 2009	3	deg		avg 1 h		3°
Wind direction	R.M. Young anemometer 05103	Aug 2009	…	3	deg		avg 30 min		3°

[1] average
[2] from [M/YYYY]

Variable	Sensor	Period of operation from	to	Height [m]	Unit	Measuring interval	Integration method	Spectral range	(Field) accuracy [±]
Windspeed	R.M. Young anemometer 05103	Sep 1998	Aug 2009	3	ms^{-1}		avg 1 h		0.3 ms^{-1}
Windspeed	R.M. Young anemometer 05103	Aug 2009	…	3	ms^{-1}		avg 30 min		0.3 ms^{-1}
Net radiation	CS[3] Q7	Sep 1998	Apr 2000	1.14	Wm^{-2}	20 s	avg 1 h	0.25 to 60 µm	6-10 %
Net radiation	Kipp & Zonen NR-LITE	Apr 2000	May 2002	4/2000: 1.14 9/2003: 1.6	Wm^{-2}	20 s	avg 1 h	0 to 100 µm	3-20 %
Net radiation	CS Q7	May 2002	Sep 2003	1.14	Wm^{-2}	20 s	avg 1 h	0.25 to 60 µm	6-10 %
Net radiation	Kipp & Zonen NR-LITE	Sep 2003	Aug 2009	4/2000: 1.14 9/2003: 1.6	Wm^{-2}	20 s	avg 1 h	0 to 100 µm	3-20 %
Incoming shortwave radiation	Skye Pyranometer SP1110	Sep 1998	Aug 2009	2	Wm^{-2}	20 s	avg 1 h	350 nm to 1100 nm	5 % (typically <±3 %)
Outgoing longwave radiation	Kipp & Zonen Pyrgeometer CG1	May 2002	Aug 2009	5/2002: 2.0 9/2003: 1.6	Wm^{-2}	20 s	avg 1 h	4.5 to 42 µm (50% points)	10 % for daily totals
Four components radiation	Huxeflux NR01	Aug 2009	…	1.56	Wm^{-2}	60 s	avg 30 min	305 to 2800 nm[4]; 4500 to 50000 nm[C]	10 % for daily sums

[3] Campbell Scientific Ltd.
[4] 50% transmission points

Variable	Sensor	Period of operation from	to	Height [m]	Unit	Measuring interval	Integration method	Spectral range	(Field) accuracy [±]
Precipitation	Young 52203 unheated Tipping Bucket Rain Gauge	Sep 1998	July 2010	1.68	mm		sum 1 h		2 % (up to 25 mm/hour)
Precipitation	Young 52203 unheated Tipping Bucket Rain Gauge	July 2010	…	1.68	mm		sum 30 min		2 % (up to 25 mm/hour)
Snow sensors									
Snowdepth	CS SR50 ultrasound	Sep 1998	Aug 2009	9/1999: 2.00 7/2001: 1.60 9/2003: 1.45	m		single 12 h		1 2.5 cm
Snowdepth	CS SR50 ultrasound	Aug 2009	…	1.45	m		single 30 min		1 2.5 cm
Snowdepth @eddy covariance site	CS SR50 ultrasound	Mar 2007	…	2.4	m	3 min	avg 1 h		1 2.5 cm
Snowdepth	Jenoptik SHM30 laser distance	Aug 2013	…		m		single 0.5 h		5 mm
Air/snow temperature	3x PT100	Aug 1999	Aug 2009	8/1999: 0.20; 0.35; 0.48 9/2003: 0.01; 0.20; 0.48 9/2004: 0.01; 0.20; 0.35	°C	15 min	avg 1 h		0.1 °C

Variable	Sensor	Period of operation from	to	Height [m]	Unit	Measuring interval	Integration method	Spectral range	(Field) accuracy [±]
Air/snow temperature	2x PT100	Aug 2009	…	0.04; 0.2	°C	60 s	avg 30 min		0.1 °C
Snow dielectric number	TDR Tektronix 1502B, SDM50 Multiplexer, 1x TDR triple wire 0.5m	Sep 1998	Dec 2009	0 to 0.5 (vertical)			single 1 h		
Snow dielectric number	TDR100, SDM50 Multiplexer, 1x CS605 probes, triple wire 0.3 m	Aug 2009	…	0 to 0.3 (vertical)			single 1 h		
Soil sensors									
Soil temperature (2D), profile (a)	32x CS 107	Sep 1998	Jan 2012	-0.045 to -1.25[5]	°C		single 1 h		0.1 °C
Soil temperature (1D), profile (c)	8x CS 107	Aug 2009	…	-0.01 to -1.41[6]	°C	60 s	avg 1 h		0.1 °C
Soil temperature (1D), profile (b)	6x PT100	Aug 1999	Aug 2009	-0.02 to -1.43[7]	°C	15 min	avg 1 h		0.1 °C

[5] See ~~a~~Appendix C, ~~f~~Figure C8
[6] Exact heights [m]: -0.01; -0.11; -0.21; -0.37; -0.55; -0.71; -0.89; -1.41
[7] Exact heights [m]: -0.02; -0.05; -0.24; -0.53; -0.93; -1.43

Variable	Sensor	Period of operation from	to	Height [m]	Unit	Measuring interval	Integration method	Spectral range	(Field) accuracy [±]
Soil heat flux	2x Hukseflux HFP01	Sep 1998	Dec 2012	0.18; 0.24	Wm^{-2}		single 1 h		-15 % to +5 %
Soil electrical conductivity	TDR Tektronix 1502B, SDM50 Multiplexer, 29x TDR triple wire 0.24 m long probes	Sep 1998	Dec 2009	0 to -1.2	dSm^{-1}		single 1 h		
Soil electrical conductivity	TDR100, SDM50 Multiplexer, 7x CS605 probes, triple wire 0.3 m	Aug 2009	…	-0.01 to -0.89	dSm^{-1}		single 1 h		
Soil liquid volumetric water content	TDR Tektronix 1502B, SDM50 Multiplexer, 29x TDR triple wire 0.24 m long probes	Sep 1998	Dec 2009	0 to -1.2			single 1 h		
Soil liquid volumetric water content	TDR100, SDM50 Multiplexer, 7x CS605 probes, triple wire 0.3 m	Aug 2009	…	-0.01 to -0.89			single 1 h		
Active layer and p~~P~~ermafrost temperature	Geoprecision Temperature Chain with 10 sensors, M-Log	Aug 2009	Sep 2015	0.5; 0; -0.5; -1; -1.5; -2.5; -3.5; -5.5;	°C		single 1 h		0.2 °C (absolute accuracy)

Variable	Sensor	Period of operation from	to	Height [m]	Unit	Measuring interval	Integration method	Spectral range	(Field) accuracy [±]
				-7.5; -9					
Generic sensors									
Snow/surface observation	Camera K1	Aug 2013	…	2	px		single 1 h		

Table 2. List of sensors, parameters, and instrument characteristics for the automated time series data from the Bayelva site, 1998-2017. Additional (not automated) data on snow cover and soil profiles can be found in Appendix E and Appendix F. Positive heights are above surface, negative heights are below surface.

Flag	Meaning	Description
ONL	Online data	Data from online stations, daily download, used for online status check
RAW	Raw data	Base data from offline stations, 3-monthly backup of online data, used for maintenance check in the field
LV0	Level 0	Standardised data with equal time steps, without gaps and in a standard data format
LV1	Level 1	Quality-controlled data including flags; quality control includes maintenance periods, physical plausibility, spike/constant value detection, sensor drifts and snow on sensor detection
LV2	Level 2	Modified data compiled for special purposes such as combined data series from multiple sensors and gap-filled data

Flag	Meaning	Description
0	Good data	All quality tests passed
1	No data	Missing value
2	System error	System failure led to corrupted data, e.g. when the power supply broke down, sensors were removed from their proper location, sensors broke or the data logger saved error codes
3	Maintenance	Values influenced by the installation, calibration and cleaning of sensors or programming of the data logger; information from field protocols of engineers
4	Physical limits	Values outside the physically possible or likely limits, e.g. relative humidity should be in a range of 0-100%
5	Gradient	Values unlikely because of prolonged constant periods or high/low spikes; test within each single series
6	Plausibility	Values unlikely in comparison with other series or for a given time of the year; flagged manually by engineers
7	Decreased accuracy	Values with decreased sensor accuracy, e.g. identified when freezing soil does not have a temperature of 0 °C
8	Snow-covered	Good data, but the sensor is snow-covered

Table 3. Description of data Level and quality control for data flags. Most flags are run automatically, few are done manually (for example, 3-maintainance, 6-plausibility).

Appendices

Appendix A: Symbols and abbreviations

Appendix B: Description of HRSC-AX images

Appendix C: Metadata description and pictures of climate, soil and permafrost stations, and instruments

Appendix D: Calculation and correction of soil and meteorological parameters

Appendix E: Description and data of snow profiles

Appendix F: Description and data of soil profiles

Appendix G: Names of the variables and units for data files

Appendix H: Time series plots

Appendix A: Symbols and abbreviations

R_T = measured resistance

δ_O = resistance offset at 0 °C

$\frac{L_a}{L}$ = apparent length of the TDR probes (TDR datalogger output)

ε_b = bulk dielectric number (Ka)

ε_l = temperature-dependent dielectric number of liquid water

ε_i = dielectric number of ice

ε_s = dielectric number of soil matrix

ε_a = dielectric number of air

θ_l = volumetric liquid water content

θ_i = volumetric ice content

θ_s = volume fraction of soil matrix

θ_a = volume fraction of air

θ_{tot} = total volumetric water content (liquid water and ice)

α = geometry of the medium in relation to the orientation of the applied electrical field (see Roth et al. (1990))

Φ = porosity

Z = impedance

BEC= bulk electrical conductivity

NetRad = radiation netto all [W m^{-2}]

NetRad_raw = uncorrected radiation netto all [W m^{-2}]

wind_v = wind speed [m s^{-1}]

TOC = total organic carbon [%]

SOCC = soil organic carbon content [kg m^{-2}]

CD_{bulk} = bulk carbon density [kg m^{-3}]

$\overline{\rho_{bulk}}$ = average dry bulk density [kg m^{-3}]

z = layer thickness [m]

Appendix B. Description of HRSC-AX images

HRSC is a multisensor pushbroom instrument with 9 CCD line sensors mounted in parallel (Figure B1) that has been in orbit around Mars since January 2004 on ESA's *Mars Express spacecraft* (Gwinner et al., 2016). It simultaneously obtains high-resolution stereo, multicolor, and multiphase images. Digital photogrammetric techniques are used to reconstruct the topography on the basis of five stereo channels, which provide five different views of the ground.

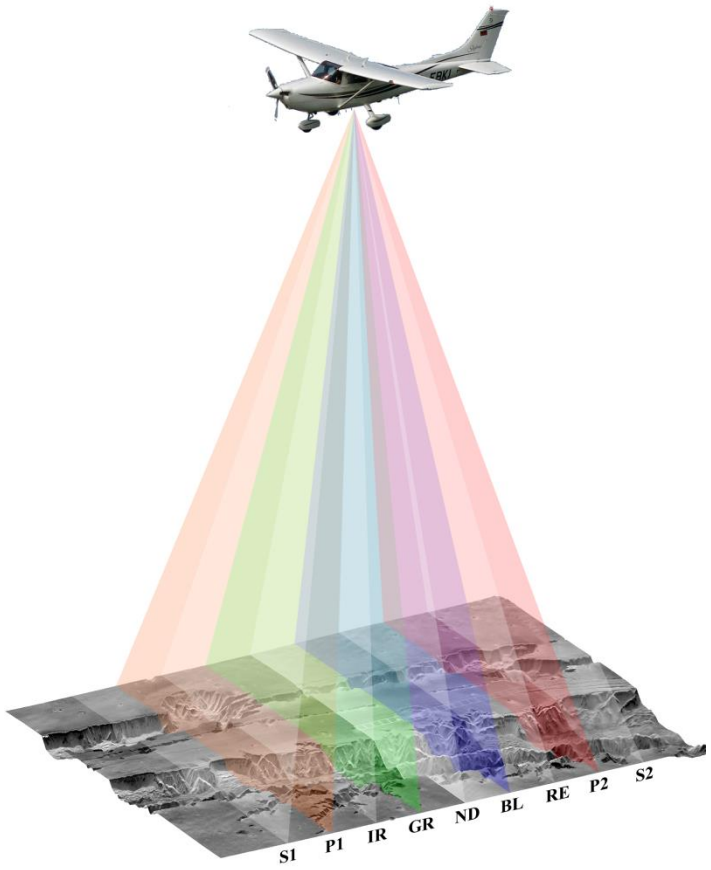

Figure B1. Operating principle of the airborne High-Resolution Stereo Camera (HRSC-AX), and viewing geometry of the individual Charge-Coupled Device (CCD) sensors. ND—nadir channel; S1, S2—stereo 1 and stereo 2; P1 and P2—photometry 1 and photometry 2; IR—near-infrared channel; GR—green channel; BL—blue channel; RE—red channel. All nine line sensors have a crosstrack field of view of ± 6 °.

The four color channels (blue, green, red, and near-infrared; Figure B2) are used to make true orthophotos in color and false color. The particular value of HRSC is the stereo capability, which allows the systematic production of high-resolution DEMs with grid sizes between 50 and 100 m (Wewel et al. (2000); Scholten and Gwinner (2004); Scholten et al. (2005); Gwinner et al. (2005, 2010).

Since 1997 different airborne versions of HRSC have been developed, one of which (HRSC-AX) was used to acquire stereo color images over Svalbard. The principles of HRSC-AX data processing are described by Gwinner et al. (2006). Data on the camera orientation are reconstructed from a global positioning system inertial navigation system (GPS INS). HRSC-AX has been used in diverse technical and scientific applications (e.g. Gwinner et al. (1999); Gwinner et al. (2000)). The aerial survey covering the Brøgger peninsula took place on 17 July 2008 at around noon, acquiring data over most of the northern part of Brøggerhalvoya (Figure B3). A Dornier Do228 aircraft from the German Aerospace Center (DLR) was used for the survey, flying at an altitude of ~2,800 m. A comprehensive description of the initial results is given by Hauber et al. (2011a, 2011b).

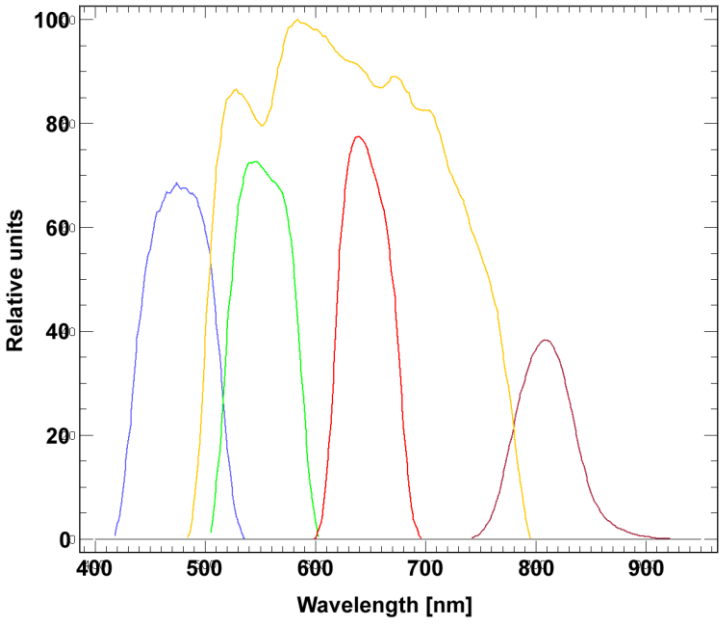

Figure B2. Spectral response of HRSC-AX panchromatic color filters.

Data processing from the raw images to the final data products, including digital photogrammetric processing, was performed with the VICAR (Video Image Communication and Retrieval; http://www.mipl.jpl.nasa.gov/external/vicar.html) software developed at the JPL (Jet Propulsion Laboratory, Pasadena, USA) and the DLR. We provide HRSC-AX data in the form of a digital elevation model (DEM) and as individual channels (panchromatic nadir channel, red, green, and blue color channels, and CIR false-color channels). The CIR (color-infrared) channels are computed by merging a false-color image (an RGB image where R, G, and B correspond to the original infrared, red, and green channels, respectively) with the nadir channel. Table B1 lists important key properties of the individual HRSC-AX image files. Metadata for HRSC-AX data are contained in "image labels", which we provide as two XML files (one for the panchromatic and (false) color images, and one for the DEM). The label entries consist of keyword-value pairs; essential keywords are defined below in Table B2. The elevations recorded in the DEM are ellipsoid heights, i.e. they are not computed with respect to a geoid but to a mathematically defined reference surface, which is a rotational ellipsoid with the equatorial A and B axes both having a radius of 6378.14 km and the polar C axis having a radius of 6356.75 ~~3356.75~~ km. This results in an offset of about 36.5 m with respect to geoid heights, i.e. sea Level in the HRSC-AX DEM is not at 0 m, but at ~36.5 m.

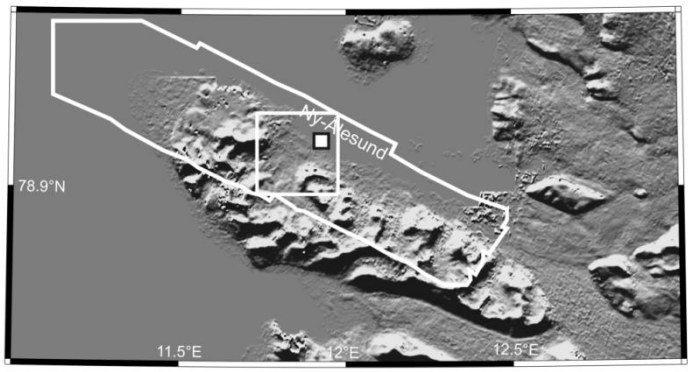

Figure B3. Context map of Brøgger peninsula, with the thick white outline showing the total coverage of the HRSC-AX survey and with the white square indicating the location of the image tile provided in this publication (base map: hillshade version of ASTER DEM).

Image name	Number of lines	Number of samples	Ground pixel size
430-8765_5.0x5.0km.pan	25,000	25,000	0.2 m
430-8765_5.0x5.0km.dsm	10,000	10,000	0.5 m
430-8765_5.0x5.0km.re	25,000	25,000	0.2 m
430-8765_5.0x5.0km.gr	25,000	25,000	0.2 m
430-8765_5.0x5.0km.bl	25,000	25,000	0.2 m
430-8765_5.0x5.0km.cir_re	25,000	25,000	0.2 m
430-8765_5.0x5.0km.cir_gr	25,000	25,000	0.2 m
430-8765_5.0x5.0km.cir_bl	25,000	25,000	0.2 m

715

Table B1. Image size and pixel size of individual HRSC-AX images.

Name	Definition	Dimension	Type	Label Group
File_Name	Name of the data file		string	
FORMAT	Image format (BYTE: 8 bit per pixel, HALF: 16 bit per pixel; REAL: 32 bit per pixel)		string	
TYPE	Type of data file		string	
ORG	Order of image file (BSQ = band sequential)		string	
NL	Number of lines		int	
NS	Number of samples		int	
NB	Number of bands		int	
TARGET_NAME	name of the target		string	MAP
A_AXIS_RADIUS	The a_axis_radius element provides the value of the semimajor axis of the ellipsoid that defines the approximate shape of a target body. 'A' is usually in the equatorial plane.	km	real	MAP
B_AXIS_RADIUS	The b_axis_radius element provides the value of the intermediate axis of the ellipsoid that defines the approximate shape of a target body. 'B' is usually in the equatorial plane.	km	real	MAP
C_AXIS_RADIUS	The c_axis_radius element provides the value of the c_axis of a solar system body. For tri-axial ellipsoidal objects, the c_axis is the semiminor axis of the ellipsoid which defines the approximate shape of the body.	km	real	MAP
BODY_LONG_AXIS_LONGITUDE	The BODY_LONG_AXIS_LONGITUDE element represents the offset between the longest axis of the triaxial ellipsoid used to model a body and the prime meridian of the body. Its value is the sum of the offset added to the prime meridian. This term is the positi	deg	real	MAP
CARTESIAN_AZIMUTH	The cartesian_azimuth element provides the clockwise rotation, in degrees, of the line and sample coordinates with respect to the center of the pixel at the map projection origin (*i.e.* where line_projection_offset and sample_projection_offset are measured).	deg	real	MAP
CENTER_LATITUDE	The center_latitude element provides a reference latitude for certain map projections. In many projections, the center_latitude along with the center_longitude defines the point or	deg	real	MAP

Name	Definition	Dimension	Type	Label Group
	tangency between the sphere of the planet and the plane of the projection.			
CENTER_LONGITUDE	The center_longitude element provides a reference longitude for certain map projections. In many projections, the center_longitude along with the center_latitude defines the point or tangency between the sphere of the planet and the plane of the projection.	deg	real	MAP
COORDINATE_SYSTEM_NAME	Defines whether the CENTER_ LATITUDE is geocentric or geodetic.		string	MAP
LINE_PROJECTION_OFFSET	The line_projection_offset element provides the line offset value of the map projection origin position from the center of the pixel at line and sample position 1,1 (line and sample 1,1 is considered the upper left corner of the digital array).	pixel	real	MAP
SAMPLE_PROJECTION_OFFSET	The sample_projection_offset element provides the sample offset value of the map projection origin position from the center of the pixel line and sample 1,1 (line and sample 1,1 is considered the upper left corner of the digital array). Note that the posi	pixel	real	MAP
MAP_PROJECTION_TYPE	The map_projection_type element identifies the type of projection characteristic of a given map.		string	MAP
MAP_SCALE	The map_scale element identifies the scale of a given map. The scale is defined as the ratio of the actual distance between two points on the surface of the target body to the distance between the corresponding points on the map. The map_scale references	km pixel^{-1}	real	MAP
POSITIVE_LONGITUDE_DIRECTION	The positive_longitude_direction element identifies the direction of longitude (e.g. EAST, WEST) for a planet. The IAU definition for direction of positive longitude is adopted.		string	MAP
SPHERICAL_AZIMUTH	One of three Euler angles (the others are center_latitude and center_longitude) that define the pre-mapping orientation of the planetary sphere for any spherical projection.		real	MAP
DTM_RANGE	indicates at which minimum or maximum value the elevations in the DTM raster file have been cut-off		real (2)	H

Name	Definition	Dimension	Type	Label Group
DTM_A_AXIS_RADIUS	The DTM_A_AXIS_RADIUS element provides the value of the (+X) semi-axis length of the triaxial ellipsoid surface used as reference for DTM data.	km	real	DIGITAL_TERRAIN_MODEL
DTM_B_AXIS_RADIUS	The DTM_B_AXIS_RADIUS element provides the value of the (+Y) semi-axis length of the triaxial ellipsoid surface used as reference for DTM data.	km	real	DIGITAL_TERRAIN_MODEL
DTM_C_AXIS_RADIUS	The DTM_C_AXIS_RADIUS element provides the value of the (+Z) semi-axis length of the triaxial ellipsoid surface used as reference for DTM data.	km	real	DIGITAL_TERRAIN_MODEL
DTM_OFFSET	The DTM_OFFSET element provides the constant value by which a stored elevation value is shifted or displaced.	m	real	DIGITAL_TERRAIN_MODEL
DTM_SCALING_FACTOR	The DTM_SCALING_FACTOR element provides the constant value by which the stored elevation is multiplied		real	DIGITAL_TERRAIN_MODEL
DTM_DESC	The DTM_DESC provides a free form, unlimited length character string that describes the DTM data.			DIGITAL_TERRAIN_MODEL

Table B2. Description of metadata (keyword-value pairs) contained in the HRSC-AX image headers.

Appendix C: Metadata description and pictures of climate, soil and permafrost stations, and instruments

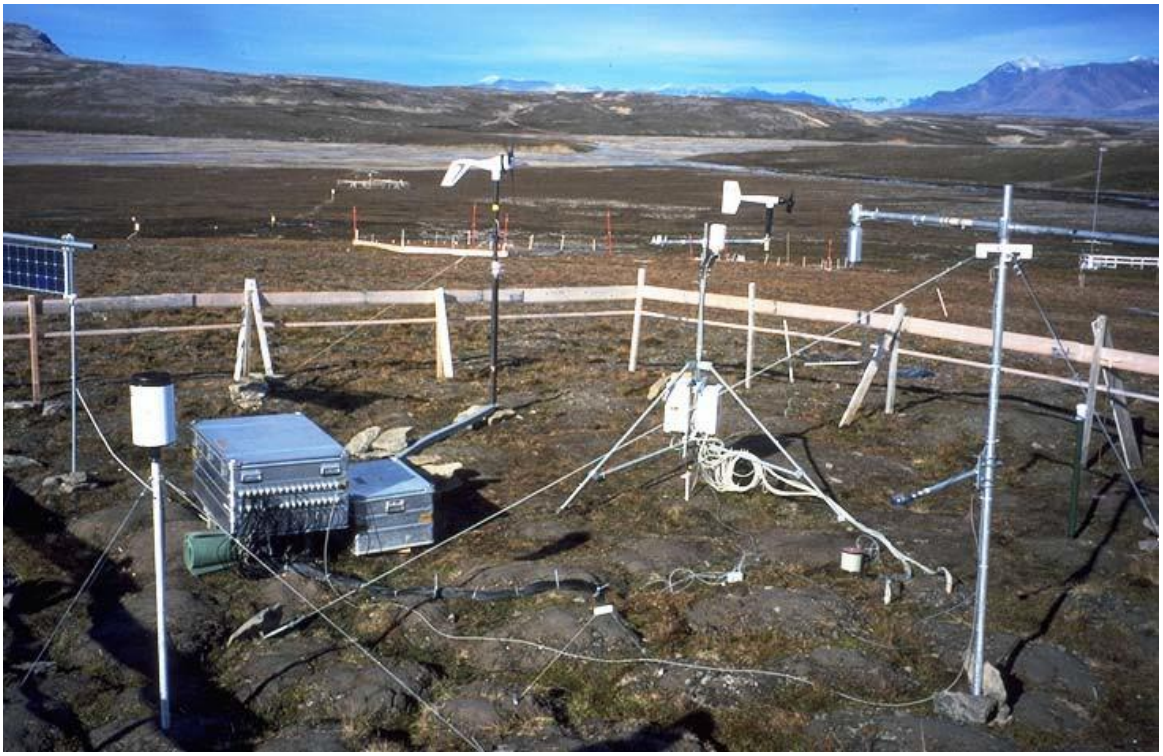

Figure C1. Bayelva climate station set up, Sept. 1998–Aug. 2009, UTM: 33 N 432100 8762992. Picture taken after installation in August 1998.

Figure C2. Climate station, Bayelva, Sept. 1998–Aug. 2009. **(a)** radiation/snow tower, **(b)** meteorological tower, **(c)** snowheight (from Sep 1999: 2 m. from Jul 2001, 1.6 m, from Sep 2003:1.45 m), **(d)** temperature/relative humidity (2 m) and temperature (1 m), **(e)** raingauge (1.68 m top of bucket above ground Level), **(f)** pyrgeometer (from May 2003: 2 m; from Sep 2003: 2 m) installed in May 2002, **(g)** net radiometer (from Apr 2000: 1.14 m; from Sep 2003: 1.6 m), **(h)** windspeed/-direction (3 m), **(i)** net radiation (from Apr 2000:1.14 m, from Sep 2003: 1.6 m), **(j)** pyranometer (2 m), **(k)** camera (2 m) with flash since Aug 2013; sensor details can be found in Table 2.

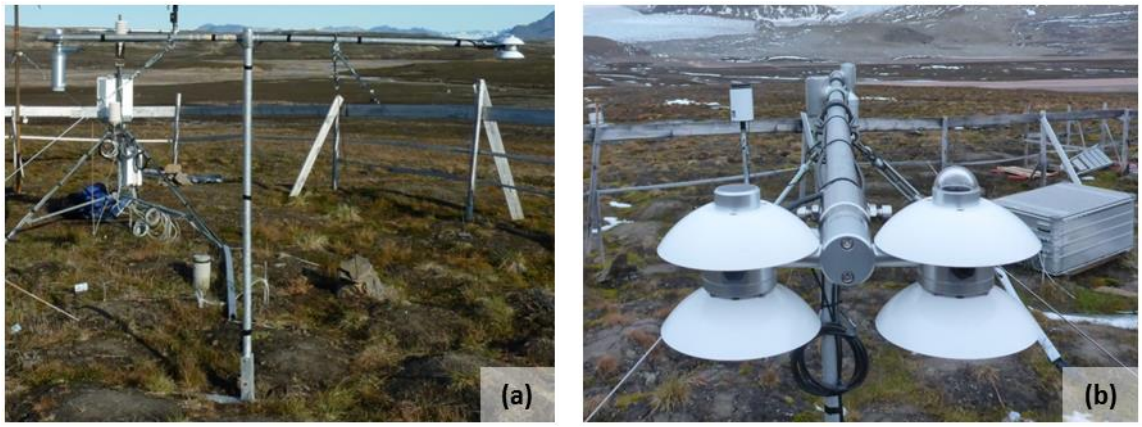

730

Figure C3. Climate station, Bayelva, Oct. 2009–present (with sensor heights), UTM: 33 N 432100 8762992. **(a)** radiation/snow tower, **(b)** four components radiation (1.56 m).

Figure C4. Laser snow depth sensor attached to the climate station, Bayelva, Aug. 2013–present, UTM: 33 N 432100 8762992.

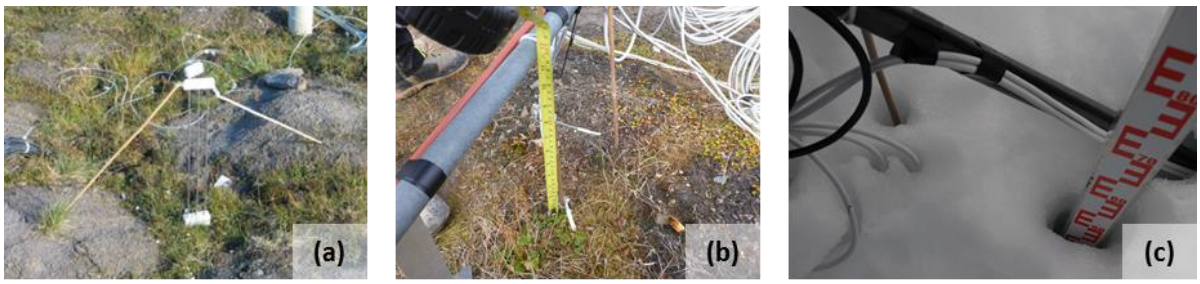

Figure C5. (a) Vertically installed time-domain reflectometry (TDR) air/ snow TDR probe (50 cm length) above the ground surface during summer at the Bayelva climate station (1999). During winter (fully snow covered), the dielectric number of snow is recorded. **(b)** PT100 temperature sensors in air (summer) at 4 and 20 cm above ground surface, **(c)** PT100

temperature sensors in snow (winter) with air gaps around cables and sticks; the TDR probe is completely covered with snow and not visible from the surface.

735

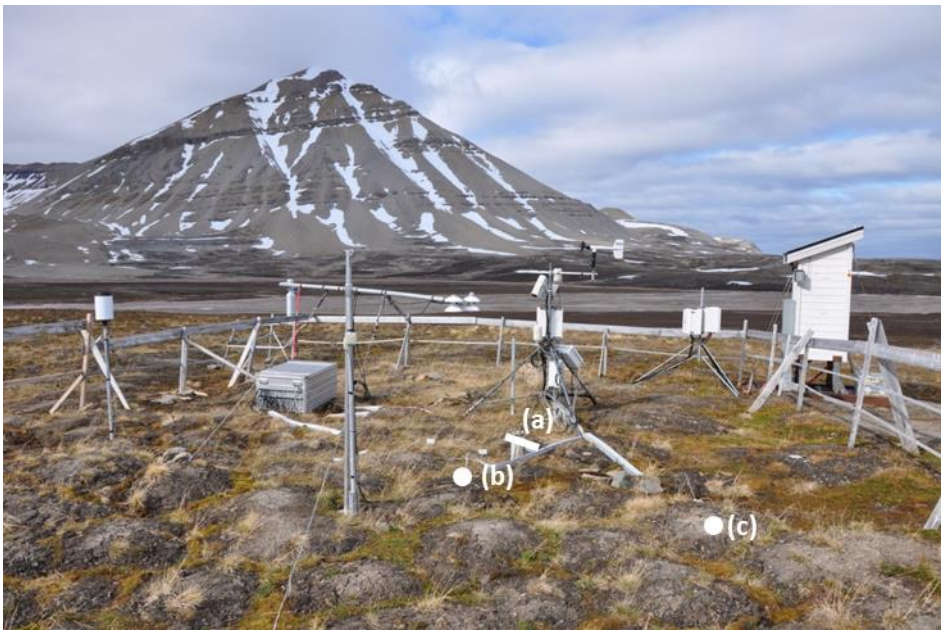

Figure C6. Location of soil profiles, Bayelva, 1998, 1999 and 2009, UTM: 33 N 432100 8762992. **(a)** 2D soil profile and station location 1998 (installed August 1998), **(b)** 1D soil station 1999 (installed July 1999), **(c)** 1D soil profile and station 2009 (installed August 2009).

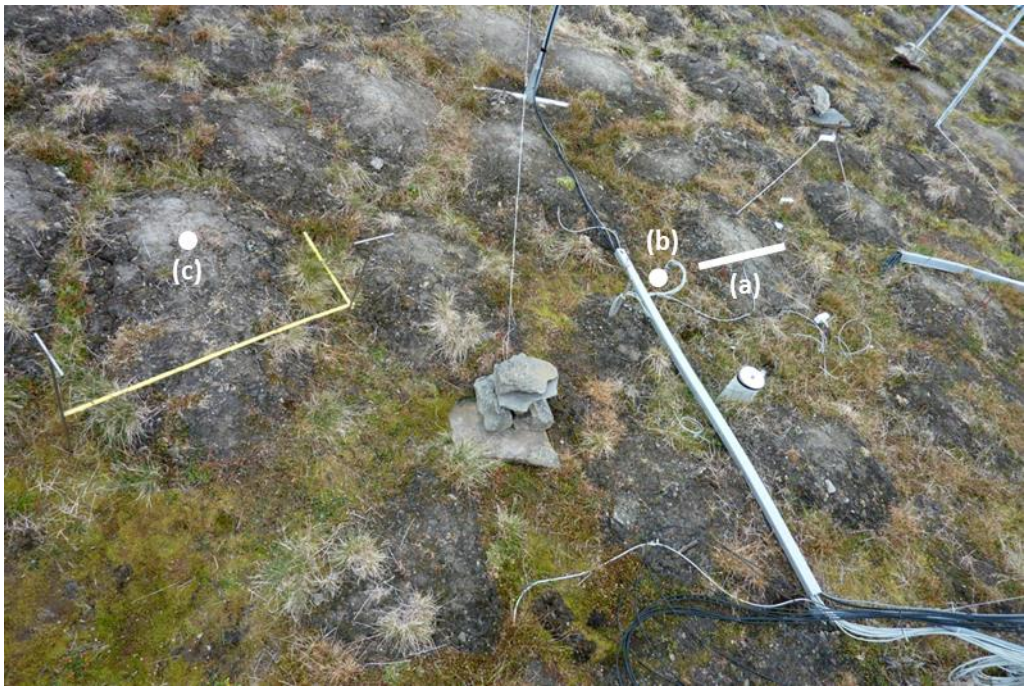

Figure C7. Soil profile and station location **(a)** 1998, **(b)** 1999, **(c)** 2009. Profile (b) upper temperature sensors were affected by reindeer disturbance in September 2003. Furthermore,

the temperature sensors were affected by continuous frost heave by about 10 cm between 2003 and 2015.

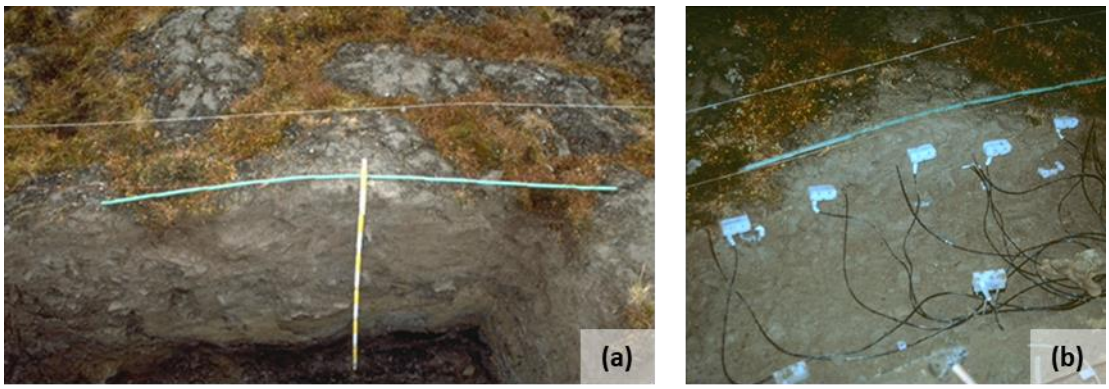

Figure C8. Bayelva soil station, Sept. 1998–January 2012, UTM: 33 N 432100 8762992. **(a)** soil profile in non-sorted circle (down to 120 cm below ground surface), **(b)** TDR and temperature probes. Soil texture and C, N, S data are listed in table F1.

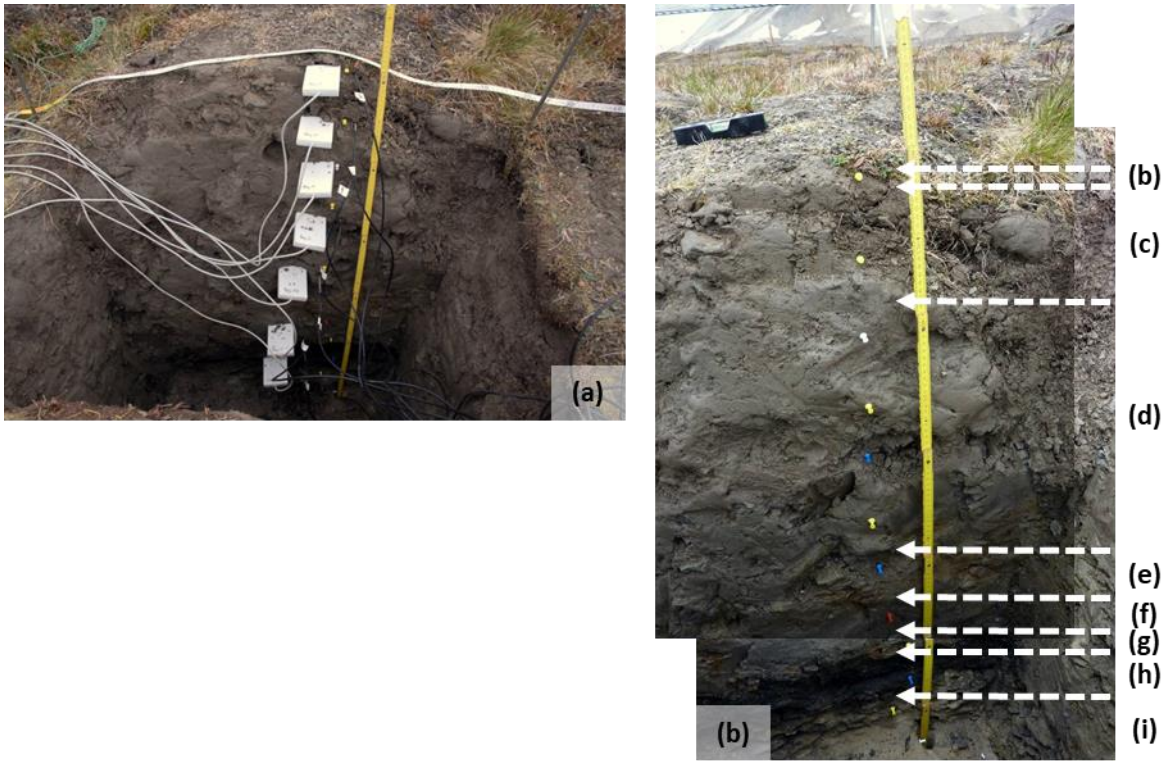

Figure C9. Bayelva soil station, Aug 2009–present, UTM: 33 N 432100 8762992. **(a)** TDR and temperature probe installation; **b:** Soil characteristics of the non-sorted circle; **(b)** moss layer (0–1 cm), **(c)** loam with roots (1–15 cm), **(d)** loam with few rocks (15–55 cm), **(e)** loam with rocks (55–65 cm), **(f)** dark loam with few rocks (65–77 cm), **(g)** rocky layer with loam

(89–95 cm), **(h)** coal layer (81–95 cm), **(i)** rocky layer (95–119 cm). Soil data for texture and C, N, S is listed in table F1.

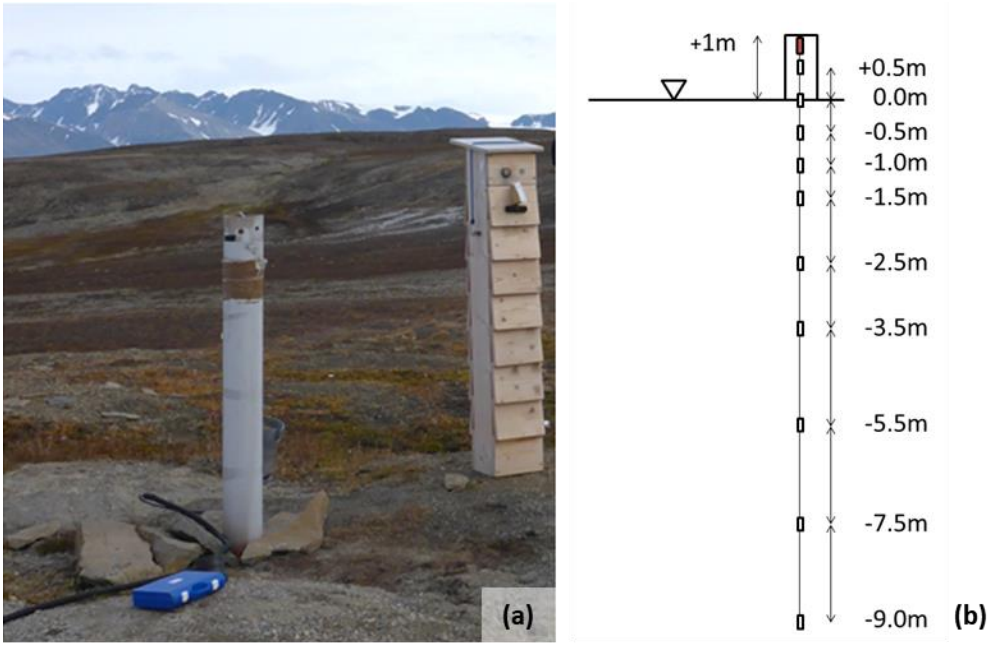

Figure C10. Borehole, Bayelva, drilled in March 2009 (total depth of 9.3 m) and instrumented in Aug 2009–present, UTM: 33 N 432118 8762978. (a) Borehole site with PVC casing outside the borehole and wooden ventilation shield removed; setup (b) with a Geoprecision temperature chain with probes at depths of 0.5 above ground surface, and 0, 0.5, 1.0, 1.5, 2.5, 3.5, 5.5, 7.5, 9 m below ground surface was used May 2009–September 2015 and May 2016–present.

Appendix D: Calculation and correction of soil and meteorological parameters

D1 Calculation of soil volumetric liquid water content using TDR

The apparent dielectric numbers were converted into liquid water content (θ_l) using the semi-empirical mixing model in (Roth et al., 1990). Frozen soil is treated as a four-phase porous medium composed of a solid (soil) matrix and interconnected pore spaces filled with water, ice and air.

The TDR method measures the ratio of apparent to physical probe rod length ($\frac{L_a}{L}$) which gives the square root of dielectric number (ε_b).

The bulk dielectric number is then calculated from the volumetric fractions and the dielectric numbers of the four phases (details in Appendix A) using

$$\varepsilon_b = [\theta_l \varepsilon_l^\alpha + \theta_i \varepsilon_i^\alpha + \theta_s \varepsilon_s^\alpha + \theta_a \varepsilon_a^\alpha]^{\frac{1}{\alpha}} \quad \text{(D1)}$$

A value of 0.5 was used for α**.**

It is not possible to distinguish between changes in the liquid water content and changes in the ice content with only one measured parameter (ε_b). Equation D1 was therefore rewritten in terms of the total water content (θ_{tot}) and the porosity (Φ) as

$$\theta_i = \theta_{tot} - \theta_l \quad \text{(D2)}$$

We remark that equation D2 assumes the densities of liquid and frozen water to be the same. This is clearly wrong for free phases and probably also in the pore space of soils. However, the density ratio can be absorbed into the dielectric number ε_i, which we do in the following. The resulting fluctuation of ε_i is presumed to be small compared to other uncertainties.

$$\theta_s = 1 - \phi \quad \text{(D3)}$$

and

$$\theta_a = \phi - \theta_l - \theta_i = \phi - \theta_{tot} \quad \text{(D4)}$$

to obtain the equation

$$\varepsilon_b = [\theta_l \varepsilon_l^\alpha + (\theta_{tot} - \theta_l)\varepsilon_i^\alpha + (1 - \phi)\varepsilon_s^\alpha + (\phi - \theta_{tot})\varepsilon_a^\alpha]^{\frac{1}{\alpha}} \quad \text{(D5)}$$

For temperatures above a threshold freezing temperature ($T > T_f$), all water is assumed to be unfrozen (θ_{tot} equals θ_l). Equation D5 then reduces to:

$$\theta_l(T) = \frac{\varepsilon_b^\alpha - \varepsilon_s^\alpha + \phi(\varepsilon_s^\alpha - \varepsilon_a^\alpha)}{\varepsilon_l^\alpha - \varepsilon_a^\alpha} \quad if\ T > T_f \quad \text{(D6)}$$

For temperatures equal to or below the threshold freezing temperature ($T \leq T_f$) it was assumed that the total water content (θ_{tot}) remained constant and only the ratio between volumetric liquid water content (θ_l) and volumetric ice content (θ_i) changed. This is a rather bold assumption as freezing can lead to high gradients of matric potential, as well as to moisture redistribution. However, since the dielectric number of ice is much smaller than the dielectric number of liquid water, the error in liquid water content measurements is still acceptable (which is not the case for ice content measurements). Under these assumptions we obtained the following equation for calculating the liquid water content of a four-phase mixture:

$$\theta_l(T \leq T_f) = \frac{\varepsilon_b^\alpha - \varepsilon_s^\alpha + \phi(\varepsilon_s^\alpha - \varepsilon_a^\alpha) + \theta_{tot}(\varepsilon_a^\alpha - \varepsilon_i^\alpha)}{\varepsilon_l^\alpha - \varepsilon_i^\alpha} \quad \text{(D7)}$$

The error of the volumetric water content measurements using TDR probes was estimated to be between 2 and 5 %, and the precision to be better than 0.5 % (Boike and Roth, 1997).

The availability of reliable temperature data is crucial in this approach. The liquid water content is first calculated for all times when the soil temperature was above the freezing threshold, using Equation D5. When the soil temperature was below the freezing threshold the water content immediately prior to the onset of freezing was determined and used as total water content (θ_{tot}) for calculating the liquid water content during the frozen interval with Equation D7.

Since water in a porous medium does not necessarily freeze at 0 °C but at a temperature that depends on the soil type and water content, estimating the threshold temperature is a crucial part of this approach. If the freezing characteristic curve is known for the material then the threshold temperature can be determined from the soil liquid water content. To avoid interpretations of frequent freezing and thawing due to soil temperature measurement errors, short-term temperature fluctuations were smoothed by calculating the mean of a moving window with an adjustable width. The smoothed temperatures were then used to trigger the switch from one equation to the other, rather than using the original temperature time series.

D2 Calculation of soil temperatures using raw data and the Steinhart-Hart equation

Temperatures were calculated from the raw voltage data using the Steinhart-Hart equation (Steinhart and Hart, 1968) and sensor calibration at 0 °C (Appendix C). The thermistors were calibrated at 0 °C prior to installation using a de-ionized water-ice mixture, from which a thermistor-specific offset (δ_O) for the Steinhart-Hart equation was obtained using

$$\frac{1}{\mathrm{T}} = 1.28 * 10^{-3} + 2.37 * 10^{-4} * \ln(\mathrm{R_T} - \delta_\mathrm{o}) + 9.06 * 10^{-8} * (\ln(\mathrm{R_T} - \delta_\mathrm{o}))^3 \quad \text{(D8)}$$

where R_T is the measured resistance and δ_o is the resistance offset at 0 °C. The estimated precision was 2.4 x 10^{-4} °C at 0 °C with an absolute error of less than 0.1 °C, in the temperature range from -40 to +40 °C.

D3 Correction of net radiation correction for wind speed

03 Sep 1998–18 Apr 2000

Campbell Scientific Ltd. Q-7 Net Radiometer running from 01 Sep 1998–18 Apr 2000.

For positive fluxes (NetRad_raw > 0 W m^{-2}) the correction formula was:

$$NetRad = NetRad\_raw * 1.159 * \left(1 + \left(\frac{0.066 * 0.2 * wind\_v}{0.066 + (0.2 * wind\_v)}\right)\right) \quad \text{(D9)}$$

For negative fluxes (NetRad_raw < 0 W m^{-2}) the correction formula was:

$$NetRad = NetRad\_raw * 0.9065 * (0.00174 * wind\_v + 0.99755) \quad \text{(D10)}$$

18 Apr 2000–20 May 2002

Kipp & Zonen NR-LITE Net Radiometer running from 18 Apr 2000–20 May 2002.

The correction formula was:

$$NetRad = NetRad\_raw * 68.027 * (1 + (0.0082 * wind\_v)) \quad \text{(D11)}$$

20 May 2002–15 Sep 2003

Campbell Scientific Ltd. Q-7 Net Radiometer running from 20 May 2002–15 Sep 2003.

For positive fluxes (NetRad_raw > 0 W m^{-2}) the correction formula was:

$$NetRad = NetRad\_raw * 7.71 * \left(1 + \left(\frac{0.066 * 0.2 * wind\_v}{0.066 + (0.2 * wind\_v)}\right)\right) \quad \text{(D12)}$$

For negative fluxes (NetRad_raw < 0 W m^{-2}) the correction formula was:

$$NetRad = NetRad\_raw * 11.66 * ((0.00174 * wind\_v) + 0.99755) \quad \text{(D13)}$$

15 Sep 2003–15 Aug 2009

Kipp & Zonen NR-LITE Net Radiometer running from 15 Sep 2003–14 Aug 2009.

The correction formula was:

$$NetRad = NetRad\_raw * 68.0272 * (1 + (0.0082 * wind\_v)) \quad \text{(D14)}$$

D4 Snow depth correction for air temperature

The raw distance D_{sn_raw} obtained from the SR50 sonic sensor (Campbell Scientific Ltd.) is calculated using the speed of sound at 0 °C and is corrected with the air temperature at 2m height using the formula provided by the manufacturer:

$$\mathrm{Dsn} = \mathrm{Dsn\_raw} * \sqrt{\frac{\mathrm{T}}{273.15}} \tag{D15}$$

Appendix E: Description and data of snow profiles

Location	Date	Air temper-ature	Total snow depth	Minimum height above ground surface	Maximum height above ground surface	Snow tem-perature	Dielectric number	Density	Grain shape	Grain size	Hand hardness index
	[YYYY-MM-DD]	[°C]	[cm]	[cm]	[cm]	[°C]		[g/cm³]		[mm]	[1-6]
Bayelva	2000-04-20		80	0	0	-9.6					
	2000-04-20		80	0	10				DH	3–4	4
	2000-04-20		80	10	10	-10		403			
	2000-04-20		80	10	29					1–3	4
	2000-04-20		80	20	20	-10.9					
	2000-04-20		80	29	52				PPip	2	4
	2000-04-20		80	30	30	-11.4					
	2000-04-20		80	40	40	-12		390			
	2000-04-20		80	50	50	-12.6					
	2000-04-20		80	52	80					<1	3
	2000-04-20		80	55	55	-13.7					
	2000-04-20		80	60	60	-14.3					
	2000-04-20		80	65	65	-15					
	2000-04-20		80	70	70	-15.5		354			
	2000-04-20		80	75	75	-15.3					
	2000-04-20		80	80	80	-13.6					
Bayelva	2006-05-11		37	0	8				IFbi		6
	2006-05-11		37	8	19					1–2	
	2006-05-11		37	10	10	-1.9					

Location	Date	Air temperature	Total snow depth	Minimum height above ground surface	Maximum height above ground surface	Snow temperature	Dielectric number	Density	Grain shape	Grain size	Hand hardness index
	[YYYY-MM-DD]	[°C]	[cm]	[cm]	[cm]	[°C]		[g/cm³]		[mm]	[1-6]
	2006-05-11		37	13	13	-2.2	3.2				
	2006-05-11		37	18	18	-2.3					
	2006-05-11		37	19	19				IFil		6
	2006-05-11		37	20	27						
	2006-05-11		37	23	23	-2.8	2.2				
	2006-05-11		37	25	25			333			
	2006-05-11		37	27	27		2.1				
	2006-05-11		37	28	28	-4.0					
	2006-05-11		37	33	33	-4.6	2.2				
	2006-05-11		37	37	37	-4.7	2.2				
Ny-Ålesund	2006-05-12	-2.7	30	0	11				IFbi		6
	2006-05-12	-2.7	30	11	24						
	2006-05-12	-2.7	30	12	12	-0.6	2.3				
	2006-05-12	-2.7	30	16	16	-1.4	2.2	304			
	2006-05-12	-2.7	30	21	21	-2.3	2.2				
	2006-05-12	-2.7	30	24	30						
	2006-05-12	-2.7	30	26	26	-3.0	2.2	324			
	2006-05-12	-2.7	30	30	30	-2.7	2.1				
Bayelva	2016-05-09		64	0	15				IFbi		6
(left)	2016-05-09		64	15	15	-2.6					
(left)	2016-05-09		64	18	18		1.3				
(left)	2016-05-09		64	19	19		1.3				
(left)	2016-05-09		64	20	20	-2.2					

Location	Date	Air temper-ature	Total snow depth	Minimum height above ground surface	Maximum height above ground surface	Snow tem-perature	Dielectric number	Density	Grain shape	Grain size	Hand hardness index
	[YYYY-MM-DD]	[°C]	[cm]	[cm]	[cm]	[°C]		[g/cm³]		[mm]	[1-6]
(left)	2016-05-09		64	23	27			275			
(left)	2016-05-09		64	24	28				IFil		6
(left)	2016-05-09		64	25	25	-2	1.2				
(left)	2016-05-09		64	30	30	-1.8	1.2				
(left)	2016-05-09		64	35	35	-1.3	1.3				
(left)	2016-05-09		64	37	41			297			
(left)	2016-05-09		64	40	40	-0.9	1.2				
(left)	2016-05-09		64	43	47				IFil		6
(left)	2016-05-09		64	45	45	-0.5	1.2				
(left)	2016-05-09		64	45	49			335			
(left)	2016-05-09		64	50	50	-0.1	1.2				
(left)	2016-05-09		64	53	57			361			
(left)	2016-05-09		64	55	55	0.1	1.3				
(left)	2016-05-09		64	55	56				IFil		6
(left)	2016-05-09		64	60	60	0.1	1.4				
(left)	2016-05-09		64	60	64			388			
Bayelva	2016-05-09		64	0	15				IFbi		6
(right)	2016-05-09		64	15	15	-2.6					
(right)	2016-05-09		64	20	20	-2.2					
(right)	2016-05-09		64	23	27			294			
(right)	2016-05-09		64	24	28				IFil		6
(right)	2016-05-09		64	25	25	-2	1.3				
(right)	2016-05-09		64	30	30	-1.8	1.2				

Location	Date	Air temper-ature	Total snow depth	Minimum height above ground surface	Maximum height above ground surface	Snow tem-perature	Dielectric number	Density	Grain shape	Grain size	Hand hardness index
	[YYYY-MM-DD]	[°C]	[cm]	[cm]	[cm]	[°C]		[g/cm³]		[mm]	[1-6]
(right)	2016-05-09		64	35	35	-1.3	1.3				
(right)	2016-05-09		64	37	41			268			
(right)	2016-05-09		64	40	40	-0.9	1.2				
(right)	2016-05-09		64	43	47				IFil		6
(right)	2016-05-09		64	45	45	-0.5	1.2				
(right)	2016-05-09		64	45	49			319			
(right)	2016-05-09		64	50	50	-0.1	1.5				
(right)	2016-05-09		64	53	57			405			
(right)	2016-05-09		64	55	55	0.1	1.5				
(right)	2016-05-09		64	55	56				IFil		6
(right)	2016-05-09		64	60	60	0.1	1.4				
(right)	2016-05-09		64	60	64			372			
Bayelva	2016-05-10	1	75	0	20				IFbi		6
(left)	2016-05-10	1	75	20	44						3
(left)	2016-05-10	1	75	22	22	-2.5					
(left)	2016-05-10	1	75	24	28			390			
(left)	2016-05-10	1	75	25	25	-2.4	1.3				
(left)	2016-05-10	1	75	28	34			359			
(left)	2016-05-10	1	75	30	30	-2.3	1.3				
(left)	2016-05-10	1	75	30	34			295			
(left)	2016-05-10	1	75	35	35	-1.9	1.3				
(left)	2016-05-10	1	75	38	42			289			
(left)	2016-05-10	1	75	40	40	-1.6	1.3				

Location	Date	Air temper-ature	Total snow depth	Minimum height above ground surface	Maximum height above ground surface	Snow tem-perature	Dielectric number	Density	Grain shape	Grain size	Hand hardness index
	[YYYY-MM-DD]	[°C]	[cm]	[cm]	[cm]	[°C]		[g/cm³]		[mm]	[1-6]
(left)	2016-05-10	1	75	40	44				IFil		6
(left)	2016-05-10	1	75	44	50				IFil		6/2
(left)	2016-05-10	1	75	45	45	-1.1					
(left)	2016-05-10	1	75	46	50			400			
(left)	2016-05-10	1	75	48	50				IFil		6
(left)	2016-05-10	1	75	50	50	-0.9	1.3				
(left)	2016-05-10	1	75	50	64						1
(left)	2016-05-10	1	75	52	58			245			
(left)	2016-05-10	1	75	55	55	-0.6	1.3				
(left)	2016-05-10	1	75	58	62			275			
(left)	2016-05-10	1	75	60	60	-0.1	1.2				
(left)	2016-05-10	1	75	62	65				IFil		6
(left)	2016-05-10	1	75	64	68			438			
(left)	2016-05-10	1	75	65	65	0.0	1.4				
(left)	2016-05-10	1	75	65	75						3
(left)	2016-05-10	1	75	68	72			453			
(left)	2016-05-10	1	75	70	70	0.1	1.5				
(left)	2016-05-10	1	75	72	72		1.4				
(left)	2016-05-10	1	75	72	76			414			
(left)	2016-05-10	1	75	73	73		1.4				
(left)	2016-05-10	1	75	74	74		1.4				
(left)	2016-05-10	1	75	75	75	0.1					
Bayelva	2016-05-10	1	75	0	20				IFbi		6

Location	Date	Air temper-ature	Total snow depth	Minimum height above ground surface	Maximum height above ground surface	Snow tem-perature	Dielectric number	Density	Grain shape	Grain size	Hand hardness index
	[YYYY-MM-DD]	[°C]	[cm]	[cm]	[cm]	[°C]		[g/cm³]		[mm]	[1-6]
(right)	2016-05-10	1	75	20	44						3
(right)	2016-05-10	1	75	22	22	-2.5					
(right)	2016-05-10	1	75	23	23		1.4				
(right)	2016-05-10	1	75	24	28			340			
(right)	2016-05-10	1	75	25	25	-2.4					
(right)	2016-05-10	1	75	28	34			357			
(right)	2016-05-10	1	75	30	30	-2.3	1.3				
(right)	2016-05-10	1	75	30	34			362			
(right)	2016-05-10	1	75	35	35	-1.9	1.3				
(right)	2016-05-10	1	75	38	42			290			
(right)	2016-05-10	1	75	40	40	-1.6	1.2				
(right)	2016-05-10	1	75	40	44				IFil		6
(right)	2016-05-10	1	75	44	50				IFil		6/2
(right)	2016-05-10	1	75	45	45	-1.1	1.3				
(right)	2016-05-10	1	75	46	50			393			
(right)	2016-05-10	1	75	48	50				IFil		6
(right)	2016-05-10	1	75	50	50	-0.9	1.2				
(right)	2016-05-10	1	75	50	64						1
(right)	2016-05-10	1	75	52	58			244			
(right)	2016-05-10	1	75	55	55	-0.6	1.2				
(right)	2016-05-10	1	75	58	62			316			
(right)	2016-05-10	1	75	60	60	-0.1	1.2				
(right)	2016-05-10	1	75	62	65				IFil		6

Location	Date	Air temperature	Total snow depth	Minimum height above ground surface	Maximum height above ground surface	Snow temperature	Dielectric number	Density	Grain shape	Grain size	Hand hardness index
	[YYYY-MM-DD]	[°C]	[cm]	[cm]	[cm]	[°C]		[g/cm³]		[mm]	[1-6]
(right)	2016-05-10	1	75	64	68			395			
(right)	2016-05-10	1	75	65	65	0.0	1.3				
(right)	2016-05-10	1	75	65	75						3
(right)	2016-05-10	1	75	68	72			421			
(right)	2016-05-10	1	75	70	70	0.1	1.4				
(right)	2016-05-10	1	75	72	72						
(right)	2016-05-10	1	75	72	76			392			
(right)	2016-05-10	1	75	73	73		1.4				
(right)	2016-05-10	1	75	74	74						
(right)	2016-05-10	1	75	75	75	0.1					

Table E1. Snow data obtained from manual probing of snow profiles in spring 2000 (Bayelva), 2006 (Bayelva and Ny-Ålesund), and 2016 (Bayelva). Data include stratigraphy, temperature, dielectric number, density and information on dominant grain shape, ~~type~~, ~~and~~ size, and hand hardness index according to international snow classification (Fierz et al., 2009). Grain shape abbreviations are DH for depth hoar, IFbi for basal ice layer, IFil for horizontal ice layer, and PPip for ice pellets. Hand hardness indices are 1 for very soft, 2 for soft, 3 for medium, 4 for hard, 5 for very hard, and 6 for ice. Left and right refer to the measurement positions within the profile shown in Figure E3.

Figure ~~E11~~E1. The Bayelva site covered by snow, 7 May 2016.

Figure E1~~12~~. Snow profile taken on 9 May 2016, inside the Bayelva fenced area. The pockets/holes are the result of snow removal using a snow density cutter (100 cm^3). Snow

depth is 47 cm above a basal ice layer at the point of measurement but ranges between 47 and 49 cm. Measurements were taken to the left of the yellow folding rule (left and right profiles in Table E1). Ice layers are present 24–28 cm, 43–47 cm, and 55–56 cm above the basal ice layer, which is 15 cm thick. Further data on temperatures, dielectric numbers, and stratigraphy can be found in Table E1.

855

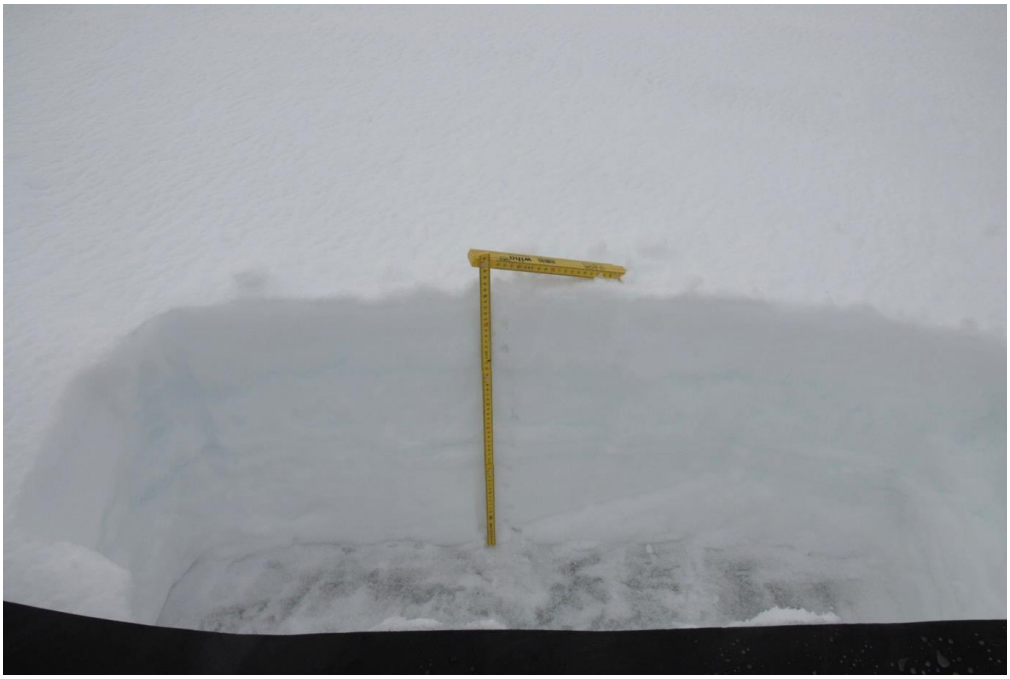

Figure E2~~13~~. Snow pit, 10 May 2016. The basal ice layer is visible at the bottom of snow layer. Two profiles were measured one to the left and one to the right from the yellow meter stick (profile data named left and right in Table E1). Further data on temperatures, dielectric numbers, and stratigraphy can be found in table E1.

Figure E3~~14~~. Measuring snow temperature in profile, 10 May 2016. Data can be found in table E1.

Appendix F: Description and data of soil profiles

Sample-ID	Date	Profile number	Depth below surface	Layer thickness	TOC	SOCC	CD_b	C	N	S	Dry bulk density	Average dry bulk density	Grain size class
	[YYYY]		[cm]	[cm]	[wt%]	[kg/m²]	[kg/m³]	[wt%]	[wt%]	[wt%]	[g/cm³]	[g/cm³]	
1/26	1998	1	11	11	1.3	2.5	22.8	1.3	< 0.1	< 0.05		1.7	sZ
1/50	1998	1	35	24	1.1	4.5	18.7	1.1	< 0.1	< 0.05		1.7	sM
1/65	1998	1	50	15	0.7	1.8		0.8	< 0.1	< 0.05		1.7	
1/76	1998	1	61	11	3.0	5.6	50.5	2.8	< 0.1	< 0.05		1.7	M
1/84	1998	1	69	8	21.2	28.9		23.8	0.4	0.4		1.7	
1/95	1998	1	80	11	4.4	8.2		4.3	0.1	0.3		1.7	
2/12	1998	2	6	6	1.1	1.1	18.2	1.2	< 0.1	< 0.05		1.7	sZ
2/37	1998	2	31	25	1.4	5.7	23.0	1.3	< 0.1	< 0.05		1.7	sZ
2/57	1998	2	51	20	1.2	4.2	20.9	1.2	< 0.1	< 0.05		1.7	sM
2/69	1998	2	63	12	1.1	2.2	18.2	1.1	< 0.1	< 0.05		1.7	M
2/78	1998	2	72	9	2.9	4.4	48.6	2.8	0.1	0.1		1.7	M
2/86	1998	2	80	8	29.4	40.0		34.3	0.6	0.6		1.7	
2/88	1998	2	82	2	4.1	1.4		4.1	0.1	0.1		1.7	
2/92	1998	2	86	4	3.8	2.6	63.9	3.7	0.1	0.2		1.7	C
3/12	1998	3	10	10	0.7	1.2	12.2	0.8	< 0.1	< 0.05		1.7	sM
3/41	1998	3	39	29	0.6	3.1	10.5	0.7	< 0.1	< 0.05		1.7	M
3/72	1998	3	70	31	1.0	5.5		1.1	< 0.1	< 0.05		1.7	
3/77	1998	3	75	5	2.7	2.3	46.4	2.7	< 0.1	< 0.05		1.7	M
3/82	1998	3	80	5	5.1	4.3	85.9	6.6	0.2	0.2		1.7	C

Sample-ID	Date	Profile number	Depth below surface	Layer thickness	TOC	SOCC	CD_b	C	N	S	Dry bulk density	Average dry bulk density	Grain size class
	[YYYY]		[cm]	[cm]	[wt%]	[kg/m²]	[kg/m³]	[wt%]	[wt%]	[wt%]	[g/cm³]	[g/cm³]	
3/92	1998	3	91	11	6.5	12.1	110.0	6.4	0.2	0.5		1.7	C
4/16	1998	4	10	10	1.3	2.2	21.8	1.3	< 0.1	< 0.05		1.7	sM
4/39	1998	4	33	23	1.0	4.1	17.7	1.0	< 0.1	< 0.05		1.7	M
4/63	1998	4	57	24	0.8	3.1	12.9	0.8	< 0.1	< 0.05		1.7	M
4/75	1998	4	69	12	0.7	1.3	11.2	0.8	< 0.1	< 0.05		1.7	M
4/88	1998	4	82	13	3.0	6.6	51.0	2.9	0.1	0.1		1.7	M
4/94	1998	4	88	6	3.7	3.7	62.1	3.4	0.1	0.1		1.7	M
5/24	1998	5	11	11	2.0	3.8	34.3	2.0	0.1	< 0.05		1.7	sZ
5/38	1998	5	25	14	1.2	2.8	19.7	1.0	< 0.1	< 0.05		1.7	sM
5/63	1998	5	50	25	1.2	5.0	19.9	1.1	< 0.1	< 0.05		1.7	M
5/75	1998	5	60	12	1.2	2.4		1.2	< 0.1	< 0.05		1.7	
5/83	1998	5	70	8	1.3	1.8	21.9	1.8	< 0.1	< 0.05		1.7	M
5/96	1998	5	83	13	3.3	7.3	56.3	3.7	< 0.1	0.1		1.7	sM
277, 299, 442	2007	1	0	0				1.3	< 0.1	< 0.05	0.8	1.5	sZ
432, 448, 470	2007	1	15	15	1.1	2.8	18.6				1.7	1.5	
259, 280, 295	2007	1	30	15	0.7	1.9	12.8				1.8	1.5	
267, 276, 453	2007	1	45	15	2.2	5.1	33.9				1.5	1.5	
454, 484, 505	2007	1	60	15	0.8	2.0	13.6				1.7	1.5	
666	2007	2	15	15				2.8	< 0.1	< 0.05	1.8	1.7	sZ
460	2007	2	30	15	1.5	3.5	23.6				1.6	1.7	
654	2007	2	45	15	1.4	3.4	22.7				1.6	1.7	
483	2007	2	60	15				2.3	< 0.1	< 0.05	1.7	1.7	sZ
290	2007	2	70	10	1.2	1.9	19.1				1.6	1.7	
480	2007	2	82	12	1.2	2.7	22.1				1.8	1.7	

Sample-ID	Date	Profile number	Depth below surface	Layer thickness	TOC	SOCC	CD_b	C	N	S	Dry bulk density	Average dry bulk density	Grain size class
	[YYYY]		[cm]	[cm]	[wt%]	[kg/m²]	[kg/m³]	[wt%]	[wt%]	[wt%]	[g/cm³]	[g/cm³]	
532	2007	2	95	13				2.9	< 0.1	< 0.05	1.7	1.7	sZ
298	2007	2	105	10	1.3	2.2	21.8				1.7	1.7	
593	2007	2	110	5				2.4	< 0.1	< 0.05	1.6	1.7	sZ
782	2007	3	15	15				2.0	0.1	< 0.05	1.4	1.5	sZ
288	2007	3	30	15	1.1	2.2	15.0				1.4	1.5	
513	2007	3	40	10	1.7	2.4	23.6				1.4	1.5	
208	2007	3	50	10	1.0	1.5	15.3	2.0	< 0.1	< 0.05	1.5	1.5	sZ
478	2007	3	65	15				1.5	< 0.1	0.1	1.4	1.5	sZ
469	2007	3	80	15	0.5	1.1	7.6				1.5	1.5	
292	2007	3	100	20	0.9	2.8	14.0				1.6	1.5	
270	2007	3	125	25				0.9	< 0.1	< 0.05	1.8	1.5	sZ
	2009	1	5	5							2.1	2.2	
	2009	1	19	19	1.3	5.6	29.5	1.8	< 0.1	0.3	2.2	2.2	sZ
	2009	1	30	11	15.7	37.7	345.8	15.4	0.4	1.0		2.2	zS
	2009	1	35	5	51.2	55.9	1126.7	45.7	1.1	1.9	2.2	2.2	Z
	2009	1	50	15	2.2	7.4	49.5	2.4	0.1	0.2		2.2	sZ
	2009	1	60	10	1.5	3.3	33.3	1.8	< 0.1	0.2		2.2	sZ
	2009	1	70	10	0.8	1.7	17.3	1.0	< 0.1	0.2		2.2	sZ
	2009	1	80	10	1.5	3.3	33.5	1.7	0.1	0.2		2.2	sZ
	2009	1	90	10	1.0	2.3	22.8	1.2	< 0.1	0.2		2.2	sZ
	2009	1	100	10	0.9	1.9	19.4	1.0	< 0.1	0.2		2.2	sZ
	2009	1	110	10	0.9	2.1	20.7	1.1	< 0.1	0.2		2.2	sZ
	2009	1	120	10	1.1	2.3	23.5	1.2	< 0.1	0.2		2.2	sZ

Table F1. Soil data from the soil pits in 1998, 2007, and 2009. The location of the soil profiles (including pictures and location) is given in Appendix C. Grain size class according to Folk (1954) with S: sand, s: sandy, Z: silt, z: silty, M: mud, m: muddy, C: clay, and c: clayey. In 2009 at depths of 30 and 35 cm high Total Organic Content (TOC)-, Soil Organic Carbon Content (SOCC)-, bulk Carbon Density (CD_{bulk})- and Carbon (C)-values possible due to natural coal in the soil profile. The soil organic carbon content (SOCC) [kg m^{-2}] has been calculated using the following formula:

$$SOCC = TOC * \overline{\rho_{bulk}} * z = \frac{CD_{bulk}}{z} \quad \text{(F1)}$$

The bulk carbon density (CD_{bulk}) [kg m^{-3}] has been calculated using the bulk soil density ρ_{bulk} and the following formula:

$$CD_{bulk} = TOC * \overline{\rho_{bulk}} = SOCC * z \quad \text{(F2)}$$

Appendix G: Names of the variables and units for data files

variable	columnname	unit
air/snow temperature	Tair_(height in cm)	°C
relative humidity	RH_(height in cm)	%
incoming shortwave radiation	SwIn	W m^{-2}
outgoing shortwave radiation	SwOut	W m^{-2}
incoming longwave radiation	LwIn	W m^{-2}
outgoing longwave radiation	LwOut	W m^{-2}
net radiation	RadNet	W m^{-2}
wind speed	Vwind_(height in cm)	m s^{-1}
wind direction	Dirwind_(height in cm)	°
wind direction standard deviation	Dirwind_sd_(height in cm)	°
soil/permafrost temperature	Ts_(depth in cm)	°C
soil bulk electrical conductivity	Cond_(depth in cm)	S m^{-1}
dielectric number	E2_(depth in cm)	–
soil volumetric liquid water content	Vwc_(depth in cm)	–
ground heat flux	G	W m^{-2}
precipitation (liquid)	Prec	mm
snow depth	Dsn	m

Table G1. Overview of all variables provided as time series. The variables electric conductivity, dielectric number, soil temperature, and volumetric soil liquid water content include a second number or letter in the column name. In these cases, the first number is the distance in the 2D profile and the second is the depth. The single letters [a, b, c, d] refer to the different 1D profiles. Vertically oriented probes are marked with letter [v]. Additional Level 2 data is provided for the variables snow depth, soil temperature, and volumetric soil liquid water content, which is indicated by "_lv2" in the column names. If an air temperature sensor is covered by snow and thus measures snow temperature, this is indicated by a flag in the data.

Appendix H: Time series plots

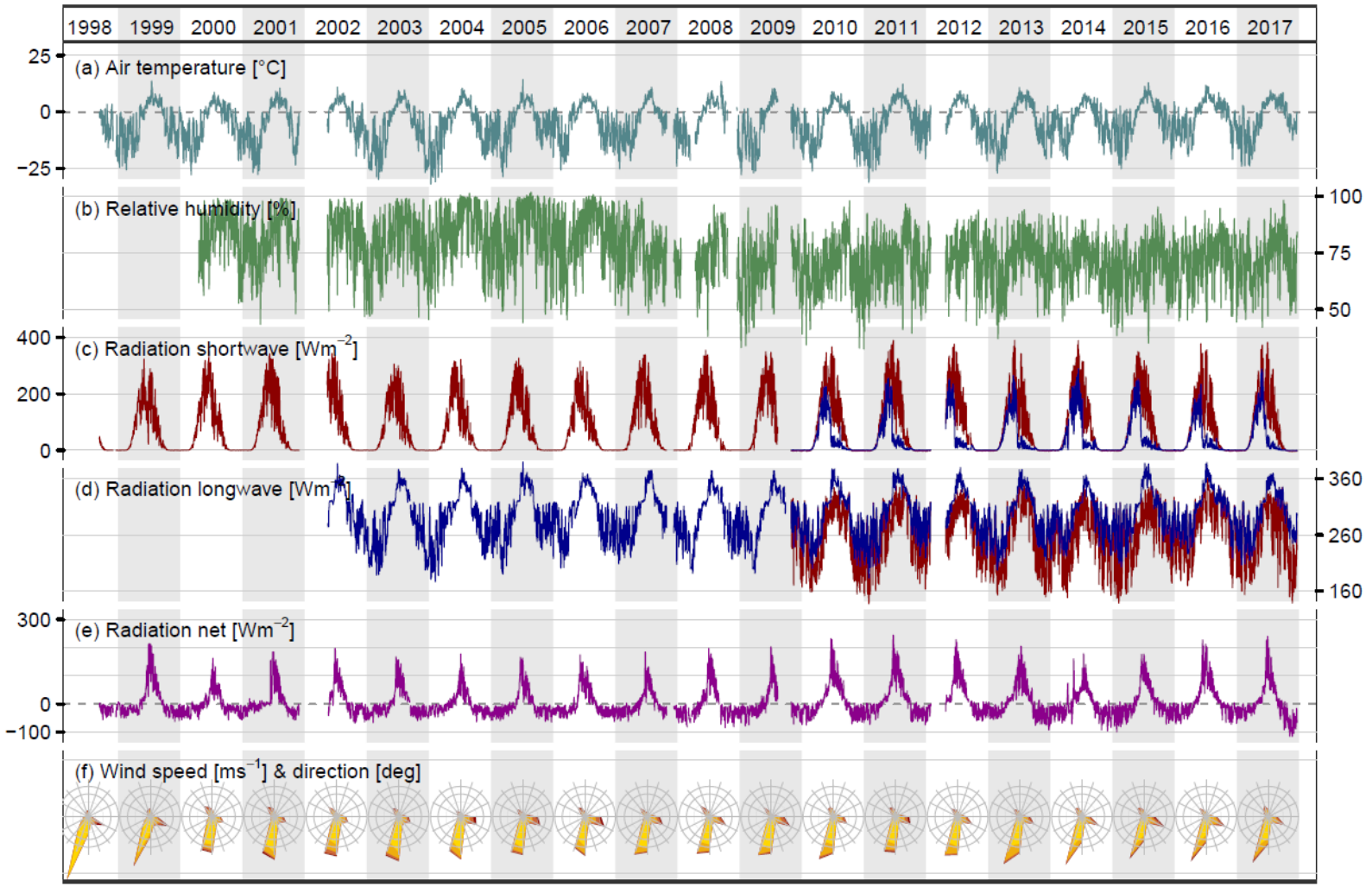
1998
1999
2000
2001
2002
2003
2004
2005
2006
2007
2008
2009
2010
2011
2012
2013
2014
2015
2016
2017
25
0
−25
(a) Air temperature [°C]
(b) Relative humidity [%]
100
75
50
400
200
0
(c) Radiation shortwave [Wm−2]
(d) Radiation longwave [Wm−2]
360
260
160
300
0
−100
(e) Radiation net [Wm−2]
(f) Wind speed [ms−1] & direction [deg]

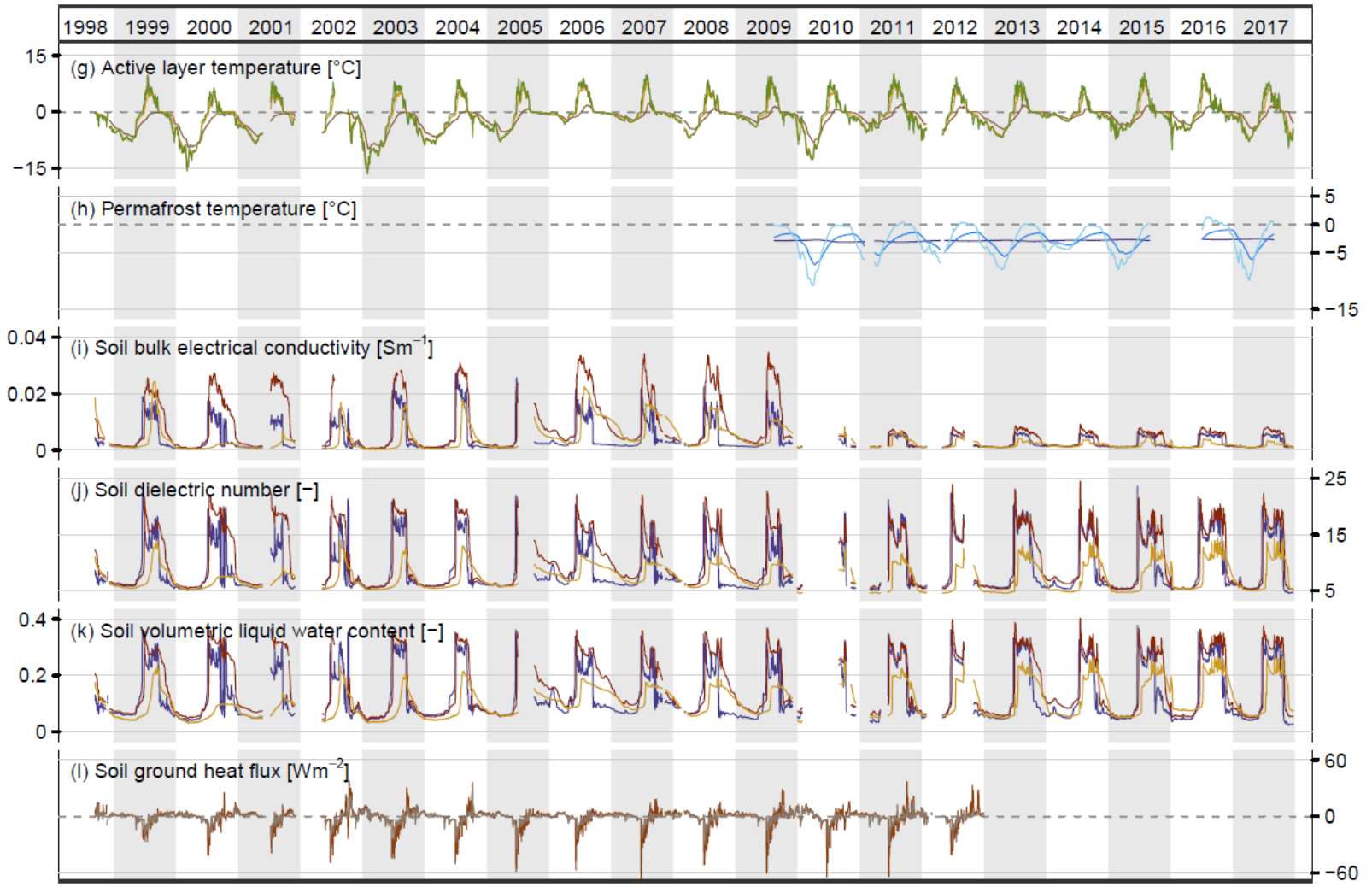
1998
1999
2000
2001
2002
2003
2004
2005
2006
2007
2008
2009
2010
2011
2012
2013
2014
2015
2016
2017
(g) Active layer temperature [°C]
15
0
−15
(h) Permafrost temperature [°C]
5
0
−5
−15
(i) Soil bulk electrical conductivity [Sm^{-1}]
0.04
0.02
0
(j) Soil dielectric number [−]
25
15
5
(k) Soil volumetric liquid water content [−]
0.4
0.2
0
(l) Soil ground heat flux [Wm^{-2}]
60
0
−60

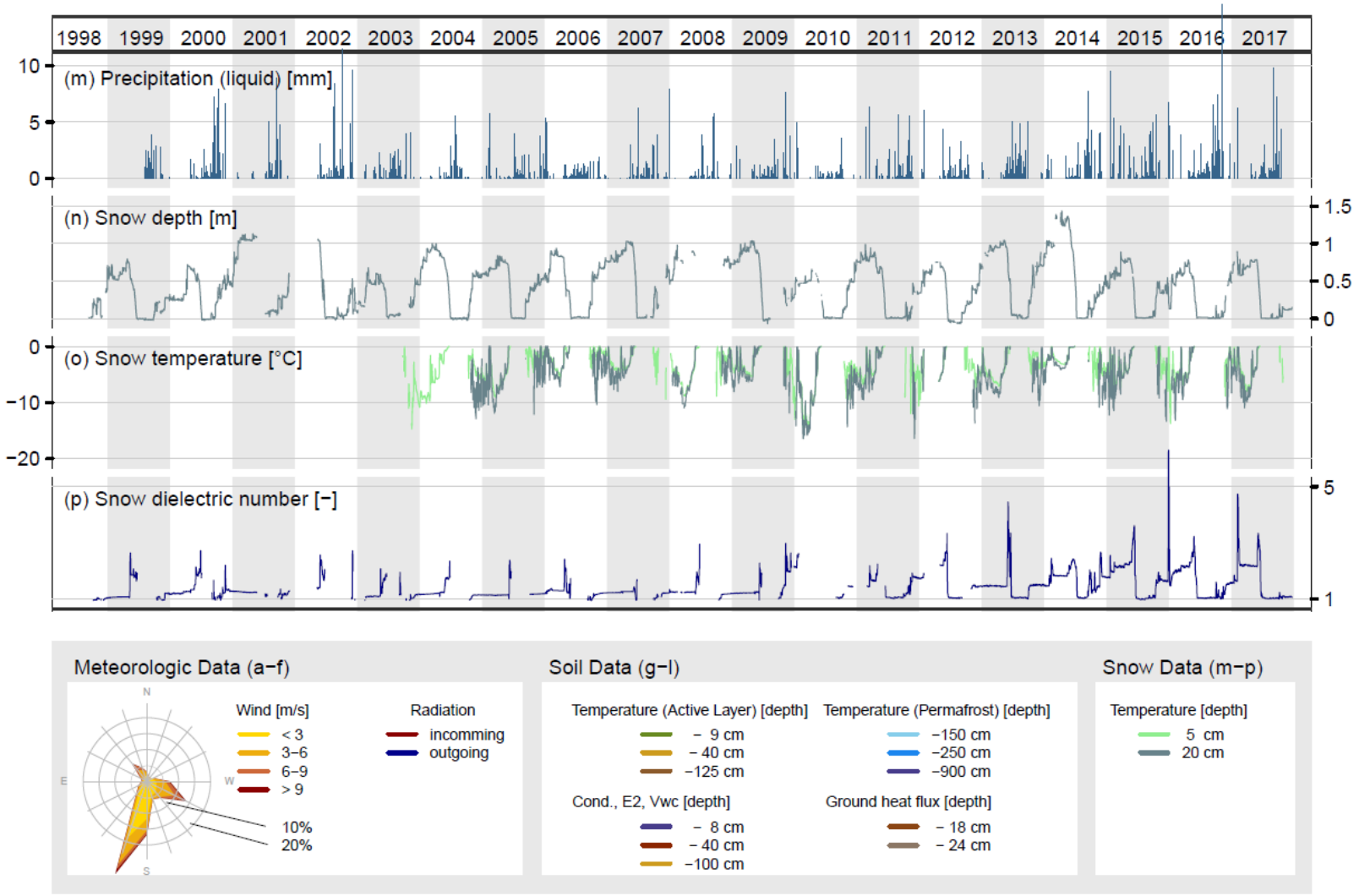
1998 1999 2000 2001 2002 2003 2004 2005 2006 2007 2008 2009 2010 2011 2012 2013 2014 2015 2016 2017
(m) Precipitation (liquid) [mm]
10
5
0
(n) Snow depth [m]
1.5
1
0.5
0
(o) Snow temperature [°C]
0
−10
−20
(p) Snow dielectric number [−]
5
1
Meteorologic Data (a−f)
N
E
W
S
Wind [m/s]
< 3
3−6
6−9
> 9
10%
20%
Radiation
incomming
outgoing
Soil Data (g−l)
Temperature (Active Layer) [depth]
− 9 cm
− 40 cm
−125 cm
Temperature (Permafrost) [depth]
−150 cm
−250 cm
−900 cm
Cond., E2, Vwc [depth]
− 8 cm
− 40 cm
−100 cm
Ground heat flux [depth]
− 18 cm
− 24 cm
Snow Data (m−p)
Temperature [depth]
5 cm
20 cm

885

Figure H1. Time series of Bayelva data provided in this paper (Figure 3) divided into three plots. a-f: meteorological data, g-l: soil/subsurface data, m-p: snow data. The data are organized following the structure of Appendix G. Further details on the sensors and periods of operation are given in Table 2.

References

Boike, J., Hinzman, L. D., Overduin, P. P., Romanovsky, V., Ippisch, O., and Roth, K.: A Comparison of Snow Melt at Three Circumpolar Sites: Spitsbergen, Siberia, Alaska, Zuerich, Switzerland2003a.

Boike, J., Ippisch, O., Overduin, P. P., Hagedorn, B., and Roth, K.: Water, heat and solute dynamics of a mud boil, Spitsbergen, Geomorphology, 95, 61-73, 2008a.

Boike, J., Langer, M., Lantuit, H., Muster, S., Roth, K., Sachs, T., Overduin, P., Westermann, S., and McGuire, A. D.: Permafrost – Physical Aspects, Carbon Cycling, Databases and Uncertainties. In: Recarbonization of the Biosphere: Ecosystems and the Global Carbon Cycle, Lal, R. (Ed.), Springer Science+Business Media, 2012.

Boike, J. and Roth, K.: Time Domain Reflectometry as a Field Method for Measuring Water Content and Soil Water Electrical Conductivity at a Continuous Permafrost Site, Permafr. Periglac. Proc., 8, 359-370, 1997.

Boike, J., Roth, K., and Ippisch, O.: Seasonal Snow Cover on Frozen Ground: Energy Balance Calculations of a Permafrost Site Near Ny-Ålesund, Spitsbergen, J. Geophys. Res., 108, 2003b.

Boike, J., Wille, C., and Abnizova, A.: Climatology and summer energy and water balance of polygonal tundra in the Lena River Delta, Siberia, J. Geophys. Res., 113, 2008b.

Brattbakk, I.: Ny-Ålesund, Brøggerhalvøya, Svalbard, K. Norske Vidensk. Selsk. Mus. Bot. avd. Trondheim, Norsk Polarinstitutt, Oslo, Vegetasjonskart, 1981.

Brown, J., Ferrians Jr, O. J., Heginbottom, J., and Melnikov, E.: Circum-Arctic map of permafrost and ground-ice conditions, National Snow and Ice Data Center/World Data Center for Glaciology, Boulder, CO, 1998.

Cannone, N., Augusti, A., Malfasi, F., Pallozzi, E., Calfapietra, C., and Brugnoli, E.: The interaction of biotic and abiotic factors at multiple spatial scales affects the variability of CO2 fluxes in polar environments, Polar Biol., 39, 1581–1596, 2016.

Cannone, N., Guglielmin, M., and Gerdol, R.: Relationships between vegetation patterns and periglacial landforms in northwestern Svalbard, Polar Biology, 27, 562-571, 2004.

CAVM-Team: Circumpolar Arctic Vegetation Map. (1:7,500,000 scale), U.S. Fish and Wildlife Service, Anchorage, USA, 2005.

Chadburn, S., Krinner, G., Porada, P., Bartsch, A., Beer, C., Belelli Marchesini, L., Boike, J., Elberling, B., Friborg, T., Hugelius, G., Johansson, M., Kuhry, P., Kutzbach, L., Langer, M., Lund, M., Parmentier, F. J., Peng, S., Van Huissteden, K., Wang, T., Westermann, S., Zhu, D., and Burke, E.: Carbon stocks and fluxes in the high latitudes: Using site-level data to evaluate Earth system models, Biogeosciences Discuss., 2017, 1–41, 2017.

Chadburn, S. E., Burke, E. J., Essery, R. L. H., Boike, J., Langer, M., Heikenfeld, M., Cox, P. M., and Friedlingstein, P.: Impact of model developments on present and future simulations of permafrost in a global land-surface model, The Cryosphere, 9, 1505-1521, 2015.

Christiansen, H. H., Etzelmüller, B., Isaksen, K., Juliussen, H., Farbrot, H., Humlum, O., Johansson, M., Ingeman Nielsen, T., Kristensen, L., Hjort, J., Holmlund, P., Sannel, A. B. K.,

Sigsgaard, C., Aakerman, J. H., Foged, N., Blikra, L. H., Pernosky, M. A., and Odegard, R.: The thermal state of permafrost in the nordic area during the international polar year 2007–2009, Permafr. Periglac. Proc., 21, 156-181, 2010.

Ekici, A., Beer, C., Hagemann, S., Boike, J., Langer, M., and Hauck, C.: Simulating high-latitude permafrost regions by the JSBACH terrestrial ecosystem model, Geoscientific Model Development, 7, 631-647, 2014.

Ekici, A., Chadburn, S., Chaudhary, N., Hajdu, L. H., Marmy, A., Peng, S., Boike, J., Burke, E., Friend, A. D., Hauck, C., Krinner, G., Langer, M., Miller, P. A., and Beer, C.: Site-level model intercomparison of high latitude and high altitude soil thermal dynamics in tundra and barren landscapes, The Cryosphere, 9, 1343-1361, 2015.

Fierz, C., Armstrong, R. L., Durand, Y., Etchevers, P., Greene, E., McClung, D. M., Nishimura, K., Satyawali, P. K., and Sokratov, S. A.: The international classification for seasonal snow on the ground, IHP-VII Technical Documents in Hydrology N°83, IACS Contribution N°1, UNESCO-IHP, Paris, 2009.

Folk, R. L.: The distinction between grain size and mineral composition in sedimentary-rock nomenclature, The Journal of Geology, 62, 344–359, 1954.

Førland, E. J., Benestad, R., Hanssen-Bauer, I., Haugen, J. E., and Skaugen, T. E.: Temperature and Precipitation Development at Svalbard 1900–2100, Advances in Meteorology, 2011, 14, 2011.

Gwinner, K., Coltelli, M., Flohrer, J., Jaumann, R., Matz, K.-D., Marsella, M., Roatsch, T., Scholten, F., and Trauthan, F.: The HRSC-AX MT. ETNA project: High-resolution orthoimages and 1 m dem at regional scale, International Archives of Photogrammetry and Remote Sensing, 36, 2006.

Gwinner, K., Hauber, E., Hoffmann, H., Scholten, F., Jaumann, R., Neukum, G., Coltelli, M., and Puglisi, G.: The HRSC-A experiment on high resolution imaging and DEM generation at the Aeolian Islands, Ann Arbor, Michigan, USA1999, 560–569.

Gwinner, K., Hauber, E., Jaumann, R., and Neukum, G.: High-resolution, digital photogrammetric mapping: A tool for Earth science, Eos, Transactions American Geophysical Union, 81, 513–520, 2000.

Gwinner, K., Jaumann, R., Hauber, E., Hoffmann, H., Heipke, C., Oberst, J., Neukum, G., Ansan, V., Bostelmann, J., Dumke, A., Elgner, S., Erkeling, G., Fueten, F., Hiesinger, H., Hoekzema, N. M., Kersten, E., Loizeau, D., Matz, K.-D., McGuire, P. C., Mertens, V., Michael, G., Pasewaldt, A., Pinet, P., Preusker, F., Reiss, D., Roatsch, T., Schmidt, R., Scholten, F., Spiegel, M., Stesky, R., Tirsch, D., van Gasselt, S., Walter, S., Wählisch, M., and Willner, K.: The High Resolution Stereo Camera (HRSC) of Mars Express and its approach to science analysis and mapping for Mars and its satellites, Plan. Space Sci., 126, 93–138, 2016.

Gwinner, K., Scholten, F., Spiegel, M., Schmidt, R., Giese, B., Oberst, J., Jaumann, R., Neukum, G., and Team, H. C.-I.: Hochauflösende Digitale Geländemodelle auf der Grundlage von Mars Express HRSC-Daten, Photogrammetrie - Fernerkundung - Geoinformation, 5, 387–394, 2005.

Hanssen-Bauer, I. and Førland, E. J.: Long-Term Trends in Precipitation and Temperature in the Norwegian Arctic: Can They be Explained by Changes in Atmospheric Circulation Patterns, Clim. Res., 10, 143-153, 1998.

Hauber, E., Reiss, D., Ulrich, M., Preusker, F., Trauthan, F., Zanetti, M., Hiesinger, H., Jaumann, R., Johansson, L., and Johnsson, A.: Landscape evolution in Martian mid-latitude regions: insights from analogous periglacial landforms in Svalbard, Geological Society, London, Special Publications, 356, 111-131, 2011a.

Hauber, E., Reiss, D., Ulrich, M., Preusker, F., Trauthan, F., Zanetti, M., Hiesinger, H., Jaumann, R., Johansson, L., Johnsson, A., Olvmo, M., Carlsson, E., Johansson, H. A. B., and McDaniel, S.: Periglacial landscapes on Svalbard: Terrestrial analogs for cold-climate landforms on Mars, Geological Society of America Special Papers, 483, 177–201, 2011b.

Heimovaara, T. J. and de Water, E.: A Computer Controlled TDR System for Measuring Water Content and Bulk Electrical Conductivity'. Laboratory of Physical Geography and Soil Science, University of Amsterdam, Amsterdam, 1993.

Heimovaara, T. J., Focke, A. G., Bouten, W., and Verstraten, J. M.: Assessing Temporal Variations in Soil Water Composition With Time Domain Reflectometry, Soil Science Society America Journal, 59, 689-698, 1995.

Hodson, A., Tranter, M., Gurnell, A., Clark, M., and Hagen, J. O.: The hydrochemistry of Bayelva, a high arctic proglacial stream in Svalbard, Journal of Hydrology, 257, 91-114, 2002.

Humlum, O.: Holocene permafrost aggradation in Svalbard, Geological Society London Special Publications, 242, 119-129, 2005.

Ippisch, O.: Coupled Transport in Natural Porous Media, Doctor of Natural Sciences, Rupertus Carola University of, Heidelberg, Germany, 1-144 pp., 2001.

Isaksen, K., Benestad, R. E., Harris, C., and Sollid, J. L.: Recent extreme near-surface permafrost temperatures on Svalbard in relation to future climate scenarios, Geophys. Res. Lett., 34, 2007a.

Isaksen, K., Holmlund, P., Sollid, J. L., and Harris, C.: Three Deep Alpine-Permafrost Boreholes in Svalbard and Scandinavia, Permafr. Periglac. Proc., 12, 13-25, 2001.

Isaksen, K., Sollid, J. L., Holmlund, P., and Harris, C.: Recent warming of mountain permafrost in Svalbard and Scandinavia, Journal of Geophysical Research: Earth Surface, 112, 2007b.

Koven, C. D., Riley, W. J., and Stern, A.: Analysis of permafrost thermal dynamics and response to climate change in the CMIP5 Earth System Models, Journal of Climate, 26, 1877-1900, 2012.

Langer, M., Westermann, S., Heikenfeld, M., Dorn, W., and Boike, J.: Satellite-based modeling of permafrost temperatures in a tundra lowland landscape, Remote Sensing of Environment, 135, 12-24, 2013.

Lloyd, C. R.: The measurement and modelling of the carbon dioxide exchange at a high Arctic site in Svalbard, Global Change Biology, 7, 405-426, 2001a.

Lloyd, C. R.: On the Physical Controls of the Carbon Dioxide Balance at a High Arctic Site in Svalbard, Theoretical Applied Climatology, 70, 167-182, 2001b.

Lloyd, C. R., Harding, R. J., Friborg, T., and Aurela, M.: Surface Fluxes of Heat and Water Vapour from Sites in the European Arctic, Theoretical Applied Climatology, 70, 19-33, 2001.

López-Moreno, J. I., Boike, J., Sanchez-Lorenzo, A., and Pomeroy, J. W.: Impact of climate warming on snow processes in Ny-Ålesund, a polar maritime site at Svalbard, Global and Planetary Change, 146, 10-21, 2016.

Lüers, J. and Boike, J.: Time series of annual atmospheric CO2-fluxes above a high-arctic permafrost site, Svalbard (Norway), 2008-03 to 2009-03. Department of Micrometeorology, University of Bayreuth, 2013.

Lüers, J., Westermann, S., Piel, K., and Boike, J.: Annual CO2 budget and seasonal CO2 exchange signals at a high Arctic permafrost site on Spitsbergen, Svalbard archipelago, Biogeosciences, 11, 6307-6322, 2014.

Maturilli, M., Herber, A., and König-Langlo, G.: Climatology and time series of surface meteorology in Ny-Ålesund, Svalbard, Earth Syst. Sci. Data, 5, 155-163, 2013.

Maturilli, M., Herber, A., and König-Langlo, G.: Surface radiation climatology for Ny-Ålesund, Svalbard (78.9° N), basic observations for trend detection, Theoretical and Applied Climatology, 120, 331-339, 2014.

Maturilli, M. and Kayser, M.: Arctic warming, moisture increase and circulation changes observed in the Ny-Ålesund homogenized radiosonde record, Theor. Appl. Climatol., doi: 10.1007/s00704-016-1864-0, 2016. 1–17, 2016.

Muraoka, H., Noda, H., Uchida, M., Ohtsuka, T., Koizumi, H., and Nakatsubo, T.: Photosynthetic characteristics and biomass distribution of the dominant vascular plant species in a high Arctic tundra ecosystem, Ny-Alesund, Svalbard: implications for their role in ecosystem carbon gain, J. Plant Res., 121, 137–145, 2008.

Nordli, Ø., Przybylak, R., Ogilvie, A. E. J., and Isaksen, K.: Long-term temperature trends and variability on Spitsbergen: the extended Svalbard Airport temperature series, 1898-2012, 2014, 33, 2014.

Norwegian Polar Institute: Svalbardkartet Geology Map 207, http://svalbardkartet.npolar.no/html5/index.html?viewer=svalbardkartet.html5, last access: 22 December 2017, 2016.

Ohtsuka, T., Adachi, M., Uchida, M., and Nakatsubo, T.: Relationships between vegetation types and soil properties along a topographical gradient on the northern coast of the Brøgger Peninsula, Svalbard, Polar Biosciene, 19, 63-72, 2006.

Overduin, P. P. and Kane, D. L.: Frost Boils and Soil Ice Content: Field Observations, Permafr. Periglac. Proc., 17, 291–307, 2006.

Romanovsky, V., Isaksen, K., Drozdov, D., Anisimov, O., Instanes, A., Leibman, M., McGuire, A. D., Shiklomanov, N., Smith, S., and Walker, D.: Changing permafrost and its impacts. In: Snow, Water, Ice and Permafrost in the Arctic (SWIPA) 2017, Arctic Monitoring and Assessment Programme (AMAP), Oslo, Norway, 2017.

Romanovsky, V. E., Smith, S. L., and Christiansen, H. H.: Permafrost thermal state in the polar Northern Hemisphere during the international polar year 2007–2009: a synthesis, Permafr. Periglac. Proc., 21, 106-116, 2010.

Roth, K. and Boike, J.: Quantifying the Thermal Dynamics of a Permafrost Site Near Ny-Ålesund, Svalbard, Water Resour. Res., 37, 2901–2914, 2001.

Roth, K., Schulin, R., Flühler, H., and Attinger, W.: Calibration of Time Domain Reflectometry for Water Content Measurement Using a Composite Dielectric Approach, Water Resour. Res., 26, 2267-2273, 1990.

Schneebeli, M., Coleou, C., Touvier, F., and Lesaffre, B.: Measurement of density and wetness in snow using time-domain reflectometry, Ann. Glaciol., 26, 69–72, 1998.

Scholten, F. and Gwinner, G.: Operational Parallel Processing in Digital Photogrammetry - Strategy and Results using Different Multi-Line Cameras, 20th International Congress for Photogrammetry and Remote Sensing, Istanbul (Turkey), 408–413, 2004.

Scholten, F., Gwinner, K., Roatsch, T., Matz, K.-D., Wählisch, M., Giese, B., Oberst, J., Jaumann, R., Neukum, G., and HRSC Co-I-Team: Mars Express HRSC Data Processing - Methods and Operational Aspects, Photogramm. Eng. Remote Sensing, 71, 1143–1152, 2005.

Sepp, M. and Jaagus, J.: Changes in the activity and tracks of Arctic cyclones, Climatic Change, 105, 577-595, 2011.

Steinhart, J. S. and Hart, S. R.: Calibration curves for thermistors, Deep Sea Research and Oceanographic Abstracts, 15, 497-503, 1968.

Stern, L.: Hydraulic and Thermal properties of Permafrost in Svalbard, Analysis and Modelling using GEOtop, Master of Science, Department of Physics and Astronomy, University of Heidelberg, 73 pp., 2017.

Uchida, M., Kishimoto, A., Muraoka, H., Nakatsubo, T., Kanda, H., and Koizumi, H.: Seasonal shift in factors controlling net ecosystem production in a high Arctic terrestrial ecosystem, J. Plant Res., 123, 1-7, 2009.

Uchida, M., Nakatsubo, T., Kanda, H., and Koizumi, H.: Estimations of the annual primary production of the lichen Cetrariella delisei in a glacier foreland in the High Arctic, Ny-Ålesund, Svalbard, Polar Research, 25, 39-49, 2006.

Weismüller, J., Wollschläger, U., Boike, J., Pan, X., Yu, Q., and Roth, K.: Modeling the thermal dynamics of the active layer at two contrasting permafrost sites on Svalbard and on the Tibetan Plateau, The Cryosphere, 5, 741-757, 2011.

Westermann, S.: Sensitivity of Permafrost, Doctor of Natural Sciences PhD thesis, Combined Faculties for the Natural Sciences and for Mathematics, Ruperto-Carola University, Heidelberg, 174 pp., 2010.

Westermann, S., Boike, J., Guglielmin, M., Gisnås, K., and Etzelmüller, B.: Snow melt monitoring near Ny-Ålesund, Svalbard, using Automatic Camera Systems. PANGAEA, 2015.

Westermann, S., Boike, J., Langer, M., Schuler, T. V., and Etzelmüller, B.: Modeling the impact of wintertime rain events on the thermal regime of permafrost, The Cryosphere, 5, 945-959, 2011a.

Westermann, S., Langer, M., and Boike, J.: Spatial and temporal variations of summer surface temperatures of high-arctic tundra on Svalbard -- Implications for MODIS LST based permafrost monitoring, Remote Sensing of Environment, 115, 908–922, 2011b.

Westermann, S., Lüers, J., Langer, M., Piel, K., and Boike, J.: The annual surface energy budget of a high-arctic permafrost site on Svalbard, Norway, The Cryosphere, 3, 245-263, 2009.

Wewel, F., Scholten, F., and Gwinner, K.: High Resolution Stereo Camera (HRSC) – Multispectral 3D-Data Acquisition and Photogrammetric Data Processing, Canadian Journal of Remote Sensing, 26, 466–474, 2000.

Yen, Y.-C.: Review of thermal properties of snow, ice and sea ice, CRREL, Hanover, NH, USA, 34 pp., 1981.

Yoshitake, S., Uchida, M., Ohtsuka, T., Kanda, H., Koizumi, H., and Nakatsubo, T.: Vegetation development and carbon storage on a glacier foreland in the High Arctic, Ny-Ålesund, Svalbard, Polar Science, 5, 391–397, 2011.